Novel Nanophotonic Structures and Devices for Optical Interconnect and Lithography Applications

by

Jun Tan

A Dissertation submitted to the

Graduate School-New Brunswick

Rutgers, The State University of New Jersey

in partial fulfillment of the requirements

for the degree of

Doctor of Philosophy

Graduate Program in Electrical and Computer Engineering

written under the direction of

Professor Wei Jiang

and approved by

_____

_____

_____

_____

_____

New Brunswick, New Jersey

October, 2013

ABSTRACT OF THE DISSERTATION

Novel Nanophotonic Structures and Devices for Optical Interconnect

and Lithography Applications

By Jun Tan

Dissertation Director:
Prof. Wei Jiang

Silicon photonics witnessed spectacular progress in the past decade. Optical interconnects, low cost telecommunications and optical sensors are three main application areas.

Photonic crystal is composed of periodic scatterers. When the scatterers are of the proper size and the periodicity is on the order of wavelength, all the reflections and refractions will cancel, forming photonic band-gap forbidding light to penetrate into it. If we remove one line of the scatterers, the light will be confined in this "wire" tightly, forming a photonic crystal waveguide (PCW).

To date, most of the PCW research has been focused on the even TE-like mode. However, a PCW often has an odd TE-like mode inside the photonic band gap exhibiting the slow-light effect as well. We demonstrated a novel scheme to control the excitation symmetry for a slow-light odd-mode in a PCW, and investigated the spectral signature. An odd-mode Mach-Zehnder coupler was introduced to excite a high-purity odd-mode with 20 dB signal-to-background contrast. Assisted by a mixed-mode Mach-Zehnder coupler, slow-light mode-beating can be observed, and determine the group index of this odd-mode. With slow-light enhancement, this odd-mode can help enable miniaturized devices based on transforming mode symmetry.

The evolution of the transmission spectrum of a PCW under electro-optic tuning was studied in the band of an odd TE-like mode. The spectral signature of the interband scattering from the TM-like mode to the odd TE-like mode was characterized at various bias levels. The shift of the odd-mode band was determined. Simulations were performed

to explain the spectral shift based on electro-optic and thermo-optic effects in the active photonic crystal structures. Potential impact of interband scattering on indirect interband-transition-based optical isolators is discussed and potential remedies are offered.

Nanopatterning is one of the key steps in nano-fabrication. We applied the negative index material (NIM) to enhance the evanescent wave in the near-field region and excite surface plasmons. Superlens devices working at 193nm DUV wavelength were fabricated, imaged on the photoresist, and characterized by AFM. A series of Finite-difference time-domain (FDTD) simulations were performed to analyze the imaging mechanism of the superlens.

I will never forget the happy ECE community, the cleanroom community and my colleagues, Dr. Zhiqing Duan, Dr. Chieh-Jen Ku, Dr. Jingru Zhang, Dr. Lei Lin, Gang Liu, Yang Zhang, Rui Li, Wen-Chiang Hong, et al. Without you, my PhD life will be too boring to enjoy.

Thanks to Prof. Zoran Gajic for your advises about PhD program; To the ECE department staffs, John McCarthy, Noraida Martinez, Ora Titus, Mayra Howell, John Scafidi, Steve Orbine, et al, who treat me like a family and provide me continuous help in the past years.

Last but not lease, thanks to my family, my father Jianguo Tan, my mother Huiyu Xu, my wife Yu Zhang, and my little baby girl who is coming to the world in this June. You are the source of my constant forward momentum. Wish you all happy and healthy!

TABLE OF CONTENTS

LIST OF ILLUSTRATIONS

Chapter 1. Introduction

1.1 Background of silicon photonics

The silicon (Si) photonics research begins from the late 1980s. Some pioneering works were published by Soref and Petermann at that time [1]–[4]. Since then, this research area experienced two peaks of development. Significant progress in the passive devices research was made in 1990s [4]–[11]. And a lot of active devices and high speed optical circuitries were realized in the last decade [12].

Three groups of innovators are rolling the wheel of the development. Large companies, like Intel, IBM, HP, Bell labs-Alcatel Lucent, Cisco, Oracle, drive the demands and adopt the new technologies at the first moment. So far, they have shipped quite a few mature products, and currently they are in the stage of high volume commercialization and adopting more applications; Research institutes all around the world are carrying out stirring results. The silicon photonics related publications occupy high percentage in the field of optics; Fast growing startup corporations, like Luxtera, Kotura, Aurrion, SKORPIOS, are turning their innovation into real products.

From the technical point of view, the foundry service aids the fast development of Si photonics industry. Intel and IBM developed their own Si photonics fabrication lines; Several commercial CMOS foundries, like IME in Singapore, IMEC in Belgium, freescale and BAE in USA, are putting more efforts on developing Si photonics fabrication services. More and more users, both from academy and industry, are using them to make reliable and low-cost (high volume) Si photonics chips. Concerning low cost, companies, like OpSIS, are organizing Multi-Project Wafer (MPW) projects to

benefit both the academies and CMOS foundries. Research institutes can realize their ideas more reliably with split costs, as well as the foundries can get more customers to lower their investment for preparing their process lines for the up-coming mass-production of Si photonics chips.

1.1.1 Applications

For Si photonics, the most promising applications are in the fields of optical interconnects (used by enterprise data centers, as well as family entertainments like PC to PC and PC to HDTV high volume data transfer), low-cost telecommunications, and optical sensors (including disposable biosensors) [13].

Optical interconnect research is driven by the increasing bandwidth in data transmission, including rack-to-rack (1−100 m), board-to-board (∼50−100 cm), chip-to-chip (∼1−50 cm) and even intrachip transmission. Copper is widely used in current stage electrical interconnects. But even at small transmission distances, copper interconnects become bandwidths limited above 10 GHz due to frequency-dependent losses, such as skin effect and dielectric losses from the printed circuit board (PCB) substrate material. Furthermore, the situation will be even worse above 10 GHz by reflections and crosstalk effects [14]. In intrachip transmission, the limitations are also associated with the dimensional scaling of copper interconnects and the RC time constant associated with the shrinking dimensions. Hence, there is an industry-wide desire to reduce resistivity and the dielectric constant within the integrated circuit. Optical interconnects, which do not suffer from these problems can potentially provide an alternative solution.

Si photonics technology first found applications in fiber-optic communication. Applications are focused on the low-cost, moderate performance parts of the network. These include areas in the data center and enterprise as well as emerging optical access networks. In the current information era and data age, it is clear that the demand is extremely high and the market is large. Since the nature of the market is high volume and low cost, it is likely that low-cost options will be essential, and hence, a mass-production technology such as Si photonics, could have significant impact is in this area.

Si photonics could also play a key role in sensing applications, with bio-sensing as a promising branch. The mass-production element of Si photonics sensors is clearly attractive both to manufacturers and users of the technology. One of the potential application areas for Si-based systems is the so called lab-on-a-chip in which both reaction and analysis take place in a single device. In the future, this could be extended to include electronic intelligence, a natural benefit to the sensor application area from continuing advances in the telecommunication and optical interconnect areas. Jokerst et al. [15] have considered the integrated biosensor application areas in a host of material technologies. They see Si as a key material in this field but note that the integration and miniaturization issues are the secrets to the success. Therefore, the realization of low-cost intelligent sensors in Si photonics technology is likely to follow the evolution of other applications. Nevertheless, in the short term, components of such systems will continue to evolve, notably miniaturization of the sensing head itself.

1.1.2 Why Si?

In the relatively mature application field of telecommunication, so far, almost all the best performing components are not built by silicon. Best available lasers, modulators and photodetectors at the telecommunication wavelength are made of other materials, like InP, GaAs, InGaAs and LiNbO$_3$. Only the optical cables are based on silica material. Why do we take the trouble of switching to Si photonics?

It's because all above mentioned applications have the common driving force of low cost, which is also the first demand of all the economic activities and the secret of success for all the corporations. This requirement is likely to be satisfied in part by the leveraging of vast Si microelectronics infrastructure, and hence, the involvement of semiconductor manufacturers is the key to advancement of low-cost Si photonics. Furthermore, it is most likely that technology success will be based on a Si platform, since it is the best understood and most studied material in modern technological development, which already led to the new technology revolution. Blending optical technology with low cost CMOS semiconductor processing, Si photonics has tremendous potential as a new technology. Si photonics is a disruptive technology that enables a new breed of monolithic opto-electronic devices [21]. And actually, after the development in the past decade, the Si photonics devices are approaching their counterparts made by other materials in the performance aspect.

1.1.3 Components of Si photonic integrated circuits

As a nascent technology, Si photonics has experienced tremendous progress in the past decade. The development of the optical systems or circuits is based on the reliably improving performance of each component.

Figure 1-1 shows the schematic of the optical system applied for the telecommunication and interconnection, and its components. So far, the research of some components, such as silicon photodetectors (PDs), waveguides (known as optical "wires"), has a longer history, and the performance of these devices is approaching their III-V counterparts [16]. On the other hand, although Si lasing was predicted impossible by traditional thinking of its indirect bandgap nature, recent demonstrations are promising for on chip electrically pumped Si lasers [17-20].

Besides the components mentioned above, on-chip optical buffers are necessary to balance the arriving time of signals coming from different positions on the optical circuit. Group delays exceeding 500ps were demonstrated in a device with a footprint below 0.09mm^2 [23]. The Wavelength Division Multiplexer (WDM) is also a key component in the interconnect system. An eight-channel (de)multiplexer with 3.2nm channel spacing, within an ultracompact footprint of $250 \times 200 \mu m$ was reported, which was based on the Echelle grating [24]. As well as the cascaded MZI lattice WDM with 3.2nm channel spacing [25].

As one of the most important component, Si electro-optic modulator has witnessed significant advances. A lot of mechanisms and structures have been applied to such modulators, including MZI modulator, Micro-ring modulator, Micro-ring assisted MZI modulator, carrier depletion modulator, carrier injection modulator, carrier accumulation
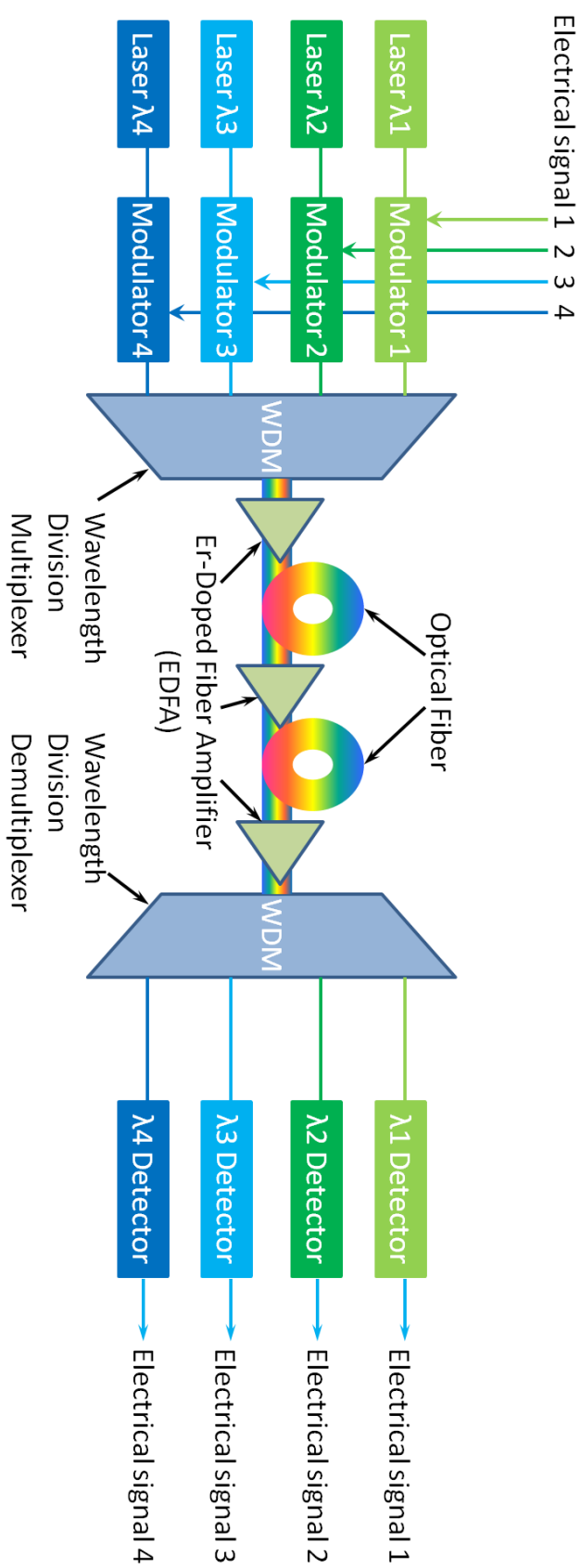
Fig. 1-1. Schematic of the optical system and its components applied for telecommunication and interconnection.

modulator, etc. [26-35].

Currently, to achieve 100 Gbps transmission speed for each interconnection link, some reported products are composed of 4 optical channels, each having the transmission capability of 25Gbps, which is a mature speed for all the components in the optical system to accomplish [22].

In the meantime, myriads of innovative Si photonic devices were developed and made into the applications. An example is the micro-ring resonator (MRR). It has passbands separated by the free spectral range (FSR) of the filter, which depends of the size of the ring. An optical signal that has been modulated onto an optical carrier can be filtered with such devices. Current fabrication technology makes it possible to realize really high optical quality factors (Q), corresponding to narrow passbands at telecommunication wavelength. MRR can also form cavities for Si Raman lasers. MRR based modulators and biosensors were heavily researched, and their performance met the application requirements [26, 36, 37].

1.2 Motivation of Si Photonic Crystal Waveguide (PCW) research

Although as aforementioned, great developments were achieved for Si photonics, in the aspects of research, products, performance, and the whole industry. It seems not adequate for meeting the growing demands. The size of typical Si photonic components integrated on optical circuits varies from several tens of microns to several hundreds of microns. Even millimeter scale devices are seen in some applications. By using the novel devices, like MRR, some components' size can be shrunk to less than 10 μm. But the working wavelength range or optical bandwidth will be limited to about 1 nm, because of

the high Q of the MRR. Thermal tuning will be required to adjust the device's working wavelength to the fitting position, which will increase the power consumption significantly.

Compared to electrical integrated circuits, which has MOS FETs with feature size as small as 22 nm for digital VLSIs produced by most advanced semiconductor technologies, optical ICs are eager for more low-cost, power efficient, compact components, to realize comparable integration density as electrical ICs.

1.3 Objectives

Photonic Crystal is one of these innovative inventions. Its sons and daughters, Photonic Crystal Cavities and Photonic Crystal Waveguides (PCWs), will facilitate the realization of different kinds of passive and active devices, with power efficient, compact features.

In recent years, great research efforts were devoted to PCWs. The fabrication processes have been well developed to make ideal 2-dimentional photonic crystals; the device performances are increasing, including high coupling efficiency, relatively low-loss; some significant new features of the PCWs were discovered, like the loss theories, light dispersion, low-light effect, enhanced light-matter interaction, etc; a lot of passive and active PCW devices were invented and characterized [68-78].

However, most of the PCW research has been focused on the TE-like mode with even symmetry. Actually, a PCW often has an odd TE-like mode inside the photonic bandgap (PBG) exhibiting the slow light effect as well. This odd mode can potentially open up the opportunities for mode-symmetry-based novel devices, such as one-way waveguides that

exploit indirect interband photonic transitions between even and odd modes. Further, compared to the even TE-like mode, the odd TE-like mode has wider bandwidth, favored by most applications. Although the group index (n_g) is smaller, it will benefit reducing the n_g related losses.

In this dissertation, we demonstrated a novel scheme to control the excitation symmetry for high purity transmission of this odd mode, and investigated the spectral signatures under various excitation symmetries. Then, the transmission characteristics under electro-optic tuning were studied. Knowledge of such active properties is important for making one-way waveguides based on electro-optically induced interband indirect photonic transition. Here we report the evolution of the PCW transmission spectrum under electro-optic tuning due to interband scattering in the spectral range of the odd mode.

Further, we discussed another novel nano-photonic device, "superlens". Our aluminum (Al) superlens working at 193 Deep Ultraviolet (UV) can amplify the near field evanescent wave, so that sub-wavelength featured can be imaged. We successfully finished the project from device fabrication to AFM characterization. Quarter wavelength feature size was achieved. This technology has potential to be used to develop new lithography tools.

1.4 Dissertation Organization

The background introduction about Si photonics is given in this Chapter 1. In Chapter 2, I will introduce the background of PCWs. Chapter 3 is based on one of our publications [93], discussing how we applied a novel approach to excite the odd TE-like

mode in a PCW and how we studied its passive properties. Followed by Chapter 4, based on another publication [115] of ours, describing the evolution of the PCW transmission spectrum under electro-optic tuning due to interband scattering in the spectral range of the odd mode. Then, the superlens project was discussed in Chapter 5, based on a working paper [127]. In the end, Chapter 6 is a summary.

Chapter 2. Introduction of the Photonic Crystal Waveguides (PCWs)

2.1 Background of photonic crystal waveguide (PCW)

Photonic crystals, analogous to solid crystals, are composed of periodic scattering centers. When the scattering centers are in the right shape and the period is on the order of the wavelength of the light, it is possible that all the reflections and refractions will cancel in the forward propagation direction and the sideway directions. And the light will be forbidden from entering the photonic crystal, no matter which direction the light is coming from. Finally, all the light will be bounced back. This happens in a certain range of wavelengths, called the photonic band gap [38].

Once we have such an opaque medium, we can manipulate photons in many interesting ways, like:

1. By carving a tunnel through the material, we have an optical "wire" from which no light can deviate. This is so far called photonics crystal waveguides (PCWs);

2. Even more dramatically, by making a cavity in the center of the crystal, we have an optical "cage" in which a beam of light could be caught and held.

These kinds of abilities to trap and guide light have many potential applications in optical communications and computing, where one would like to make tiny optical "circuits" to help manage the ever-increasing traffic through the world's optical communications networks. Other devices are also made possible by this increased control over light: from more efficient lasers and LED light sources.

In the early days of discovering the photonic crystal, some scientists proposed an optical circuit diagram composed of pure photonic crystal made devices, including modulator, WDM, photodetector, PCW, coupler, etc. But in real applications, rare optical circuits are 100% photonic crystal based. Mainly they will have both photonic crystal devices and conventional components, as you will see in the later part of this dissertation.

2.2 Experimental realization of on chip Photonic Crystal Waveguides (PCWs)

In 1998, IBM applied the silicon on insulator (SOI) technology making VLSIs. The initial purpose is to limit the leaking current into the body of CMOS by the insulator layer sandwiched between the top silicon layer and the silicon substrate, so that the power consumption will be reduced dramatically. Meanwhile, the insulator layer also lags the heat diffusion. As the heat accumulates in the electrical working areas, it will destroy the performance of the circuits.

However, this important invention was found great fitting as the platform of the on chip optical circuits used for telecommunication applications. As the top Si layer is transparent for the 1550nm telecommunication wavelength, it can be made into good waveguides, which is used as the optical "wires" for the optical circuits. The high refractive index contrast between the Si and the air or glass cladding is beneficial for tight confinement of light beams, so that compact on chip devices and systems can be achieved. The buried oxide (BOX) layer of the SOI wafers will prohibit the leakage of light into the Si substrate. It works as the bottom cladding of the Si waveguides.

In general, photonic crystal can be 1-D (Bragg grating), 2-D or 3-D. Figure 2-1 shows the diagrams about how they are arranged. This dissertation is discussing 2-D photonics crystal waveguides built in Si membrane, which is the top layer of SOI substrate. And the periodic air
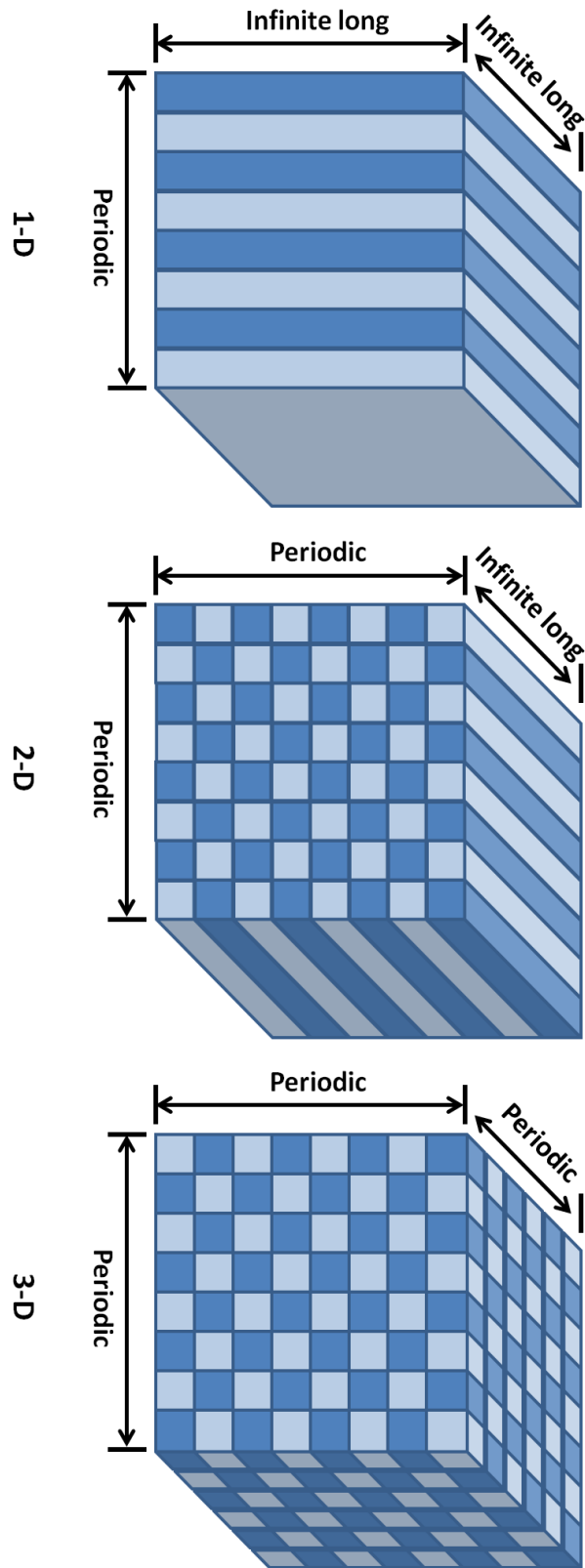
Fig. 2-1. The diagram of 1-D, 2-D and 3-D photonic crystal structures.

holes drilled in Si work as the scattering centers. Normally, researchers are focusing on square lattice and triangle lattice (same as hexagonal lattice) structures of photonic crystals. We applies hexagonal lattice in our devices.

Such photonic crystals realized on the top Si layer of SOI are named photonic crystal slabs, which are two dimensional periodic dielectric structures of finite height. Although we treat them as 2-D photonic crystals, they are actually quasi-3-D (2-D periodic with finite height). They control the light propagation by the photonic band gap (PBG) horizontally and by index confinement vertically.

To avoid the interference between different modes, almost all the on-chip optical components are designed to work in single mode condition. For wire waveguides working at 1550nm telecommunication wavelength, they are required to have thickness below 300nm and width below 500nm. The wire waveguide thickness also defines the thickness of the top Si layer in the SOI wafers. Researchers normally apply thickness varying from 220nm to 260nm. To achieve wider PBG, which is favored for most applications, the lattice constant (a) of the PhC is chosen at around 400nm and the hole radius (r) changes from $0.1a$ to $0.4a$.

Low loss of optical signal is the long-term demand of optical applications. Coupling light onto and off the optical chips efficiently is critical. Researches use single mode lensed fibers to focus light onto the edge of the optical chips, where the on-chip waveguides are precisely cleaved to and the ends are exposed to. However, the mismatch of the sizes of optical modes between the fiber and waveguide will make big trouble for efficient coupling, as the focused optical mode launched out from the lensed fiber has a waist width about 2.5 μm and the single mode Si wire waveguide has a cross-section $\sim220\times500nm^2$, which guarantees only ~0.56% geometric overlap.

What makes the problem worse is the high refractive index of the Si wire waveguides, which introduces strong reflection.

Multiple designs of spot size converter were developed to help with this problem [39-41]. A straightforward solution is waveguide taper, which expands the waveguide width and height from the wire waveguide to the sample edge, hoping it will match the mode profile of the fiber. Another design is called inverse taper, which shrinks from the normal size at Si wire waveguide to a tiny tip at the input facet. The fiber mode is coupled evanescently to the Si taper and becomes progressively more confined as the taper adiabatically widens to the final single-mode wire waveguide. The initially small effective refractive index at the input facet and the gradual refractive index change help to minimize back-reflections. But this approach needs the taper tip precisely stops at the sample edge, which will be a big challenge for sample cleaving. To overcome this difficulty, a modified inverse taper embedded in big size polymer waveguide was developed. The light beam was coupled to the polymer waveguide at the sample edge first. Then the light would couple to the high index Si wire waveguide through the inverse taper part overlapped with the polymer waveguide [42]. So far, there is no standardized approach. Researchers apply the methods they are mostly familiar with.

The light coupling from the wire waveguide to the PCW will also bring in significant loss, because the large group index of the PCW results in large impedance mismatch with the mode in the wire waveguide. This mismatch will produce strong reflection of light. Researchers are applying similar methods as mentioned above, adiabatic tapers, to solve the problem. Some researchers taper the wire waveguide to a wider width to match the PCW, while others modify the input and output parts of the PCW to lower the group index to meet that of the wire

waveguide [42-48]. Also, some researchers did theoretical studies about the mechanism of the losses happened in the PCWs [49-50].

In our devices mentioned later in this dissertation, we applied the widening taper approach to help both the fiber to wire waveguide coupling and waveguide to PCW coupling, because this will ease the fabrication significantly. And we are focusing on the signature performance of our devices, so relative improved loss is good enough for us.

Besides most commonly seen W1 PCW, which has one row of holes removed and leaves all other holes in their original positions in the hexagonal lattice, some novel PCW based devices, like slot PCW, double slot PCW, and PCW bends, were studied and interesting results were published [46, 51-53].

2.3 Useful effects in PCW

We have seen that, the PCW can tightly guide the light, so that we get a useful tool to control the light. Actually, what attract the researchers more are some other unique effects of the PCW. First of them is the slow light effect, which can slow the light velocity by a factor of tens or even hundreds times. Here, we refer the light velocity to the group velocity (v_g) of light, which carries the useful signal information.

By definition, $v_g \equiv \frac{\partial \omega}{\partial k}$. In the photonic band diagram (wavevector vs. angular frequency plot), analogous to the semiconductor electronic band structure, v_g is the slop of the photonic band. At the bandedge, the bottom of the band curve, the slop is as small as zero, which means v_g can be slowed down to zero. In experiments, it can be one hundredth of the light velocity in vacuum.

Also, because of the strong dispersion of the PCW (curving of the band), at different frequency of ω (different position of the band curve), v_g will change accordingly. So we can choose a fit frequency (wavelength) to get an ideal group velocity.

Talking about the dispersion effects in PCW, researchers want to control the shape of the band curve, to achieve large and constant curve slop (v_g) at a relatively wider bandwidth (wider frequency range). Some approaches, like changing the width of the line defect in the PCW, changing the radius of the first several rows of holes next to the line defect, and shifting the position of some particular rows of holes [54-56]. Of course, there will be some kinds of tradeoff.

Further, the slow light effect will enhance the light-matter interaction. Because the light is slowed down, the needed device length to achieve a certain interaction will be decreased significantly. This can be utilized to realize ultra-compact devices, like PCW modulators.

To characterize these features of the designed PCW, the spectra measurement is an easy and effective way. A careful measurement and analysis will bring exciting results [57]. And the small oscillations in the spectra contain important information about group velocity v_g [58].

2.4 Photonic Crystal based devices for the interconnect applications

Now, let's look at some recent publications, which designed wonderful Photonic Crystal devices to meet the interconnect application requirements.

2.4.1 Si PCW Modulators

PCW based modulators can be realized by embedding a PIN diode in the device. Using the carrier-induced plasma dispersion effect, the light intensity in the waveguide can be changed by the electrical signal driving the PIN diode. Meanwhile, the PCW structure can enhance the light-

matter interaction, so the length of the modulation part can be shrink by a factor of the group refractive index n_g, which equals c/v_g (c is the speed of light in vacuum). This design has small device footprint and ease the fabrication, along with the disadvantages, like carrier induced optical loss.

Another more popular PCW modulator design is based on the Mach-Zehnder Interferometer infrastructure [59, 60]. The PCW, integrated with the PIN diode, can be embedded in one of the two arms of the MZI, or in both arms. Thermal tuning is necessary to align the phase difference between those two arms. The modulation speed can reach 40 Gbps [60], which is sufficient to meet the applications in the next several years. The MZI structure can realize both amplitude modulation and phase modulation, so it is favored by a lot of researchers.

Most recently, researchers in Columbia University and University of California at Berkeley reported exciting results of electro-optic Si Photonic Crystal Nano-cavity modulators by electrical gating of graphene [61, 62]. I believe a new branch of Photonic Crystal research will be booming soon.

2.4.2 Si Photonic Crystal (PhC) based light source (laser or LED)

As mentioned in the previous chapter, Si light source working at the telecommunication wavelength has been in a heavy demand for a long history. A lot of approaches were developed to overcome the indirect band structure of Si. But they did not combine all of the desired characteristics of a Si light source: electrical pumping, operation at sub-bandgap wavelengths, room temperature operation, small size and narrow emission linewidth.

A couple of month ago, promising results were published about the Si Photonic Crystal based LED [63]. The researchers applied hydrogen plasma treatment to introduce nano-scale optically

active defects into Si. These defects fed the photonic crystal nanocavity to enhance the electrically driven emission. A narrow emission line ($\Delta\lambda = 0.5$ nm) at 1515 nm wavelength with a power density of 0.4 mW/cm^2 was observed. This is the highest spectral power density ever reported from any Si emitters.

This tremendous breakthrough will definitely excite the PhC researchers. And we expect to see the powerful potential in this direction.

2.4.3 WDM realized by the PhC superprism effect

WDM multiplexing and demultiplexing is a key function need for the interconnect application, as described before. At the beginning of the invention of the PhC, researchers applied the superprism effect to demonstrate the WDM devices [64-66]. Recently, the negative diffraction and negative refraction properties of the PhC were studied [67]. It was reported that a 4-channel optical demultiplexer with a channel spacing of 8 nm and cross-talk level of better than -6.5 dB was experimentally demonstrated using a 4500 μm^2 PhC region.

Chapter 3. High purity transmission of a slow-light odd mode in a photonic crystal waveguide (PCW)

3.1 Introduction

Photonic crystal waveguides (PCWs) [68-72] can modify light propagation and dispersion characteristics through their periodic structures, thus have important applications in communications and sensing. Particularly, the slow light effect in a PCW can significantly enhance the light-matter interaction [73-75], as demonstrated in significant reduction of interaction lengths for PCW based modulators and switches [76-78]. To date, most of the PCW research has been focused on the TE-like mode with even symmetry. However, a PCW often has an odd TE-like mode inside the photonic bandgap (PBG) exhibiting the slow light effect as well. This odd mode can potentially open up the opportunities for mode-symmetry-based novel devices, such as one-way waveguides that exploit indirect interband photonic transitions between even and odd modes [79]. The slow light effect in PCWs can help reduce the interaction length for such transitions, enabling ultracompact devices. To utilize this odd mode in any devices, it is crucial to control its excitation symmetry and understand its slow light spectral characteristics. Normally, this odd mode does not exhibit itself evidently in the PCW transmission spectrum because its odd symmetry prohibits its excitation from the fundamental even mode of a conventional waveguide typically used at input. Symmetry-breaking structure imperfections sometimes may induce some coupling to this odd mode, causing a decrease of PCW transmission in the odd mode band [80, 81]. Here we demonstrate a novel scheme to control the excitation symmetry for high purity transmission of this odd mode, and investigate the spectral signatures under various excitation symmetries.

3.2 Design and simulation

Consider a W1 PCW formed on a silicon-on-insulator (SOI) wafer by removing a row of air holes in a hexagonal lattice with lattice constant a=400 nm, hole radius r=0.325a, and Si slab thickness t=260 nm. The band diagram in Fig. 3-1(a) is calculated by 3D plane wave expansion [82, 83]. Below the lightline (for the oxide bottom cladding), the even TE-like mode has a flat dispersion relation with group index n_g > 50, and a narrow bandwidth (<4 nm). In contrast, below the lightline, the odd TE-like mode has a much wider bandwidth ~20 nm with n_g down to ~15. Such a moderate n_g range is favorable for many applications as various types of losses are reduced at lower n_g [72, 82, 84, 85]. Furthermore, the dispersion relation of the TM-like guided mode usually crosses that of the even mode [72], as seen in Fig. 3-1(a). But the TM-like mode does not cross the odd mode in the region below the lightline in Fig. 3-1(a). For the frequency range $\omega a/2\pi c$=0.28~0.286, only the odd mode is below the lightline.

Systematic simulations show that as the hole radius increases, the odd-mode bandedge moves up faster than the TM cutoff, as shown in Fig. 3-2. For a sufficiently large r, the TM cutoff is below the odd mode bandedge; thus the two modes do not cross each other below the lightline, helping avoid their inter-coupling due to asymmetric top and bottom claddings. However, as r increases, the transmission bandwidth bounded by the bandedge and the cutoff decreases for both the even and odd modes, as shown in Fig. 3-2. Hence, this work focuses on the intermediate r case shown in Fig. 3-1(a), which shows a sufficient clearance between the odd mode bandedge and the TM cutoff, and a sufficiently wide bandwidth.
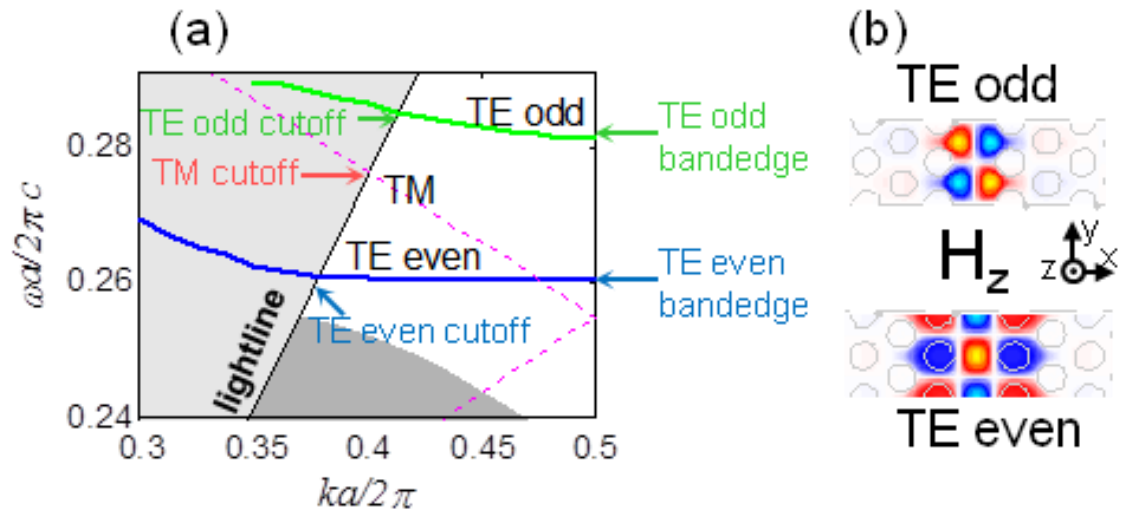
Fig. 3-1. PCW photonic band structures. (a) Band diagram for $r=0.325a$. The dark grey region indicates the lower photonic band. (b) H_z field profiles for even and odd modes at $k=\pi/a$ (PCW axis along y). [93]
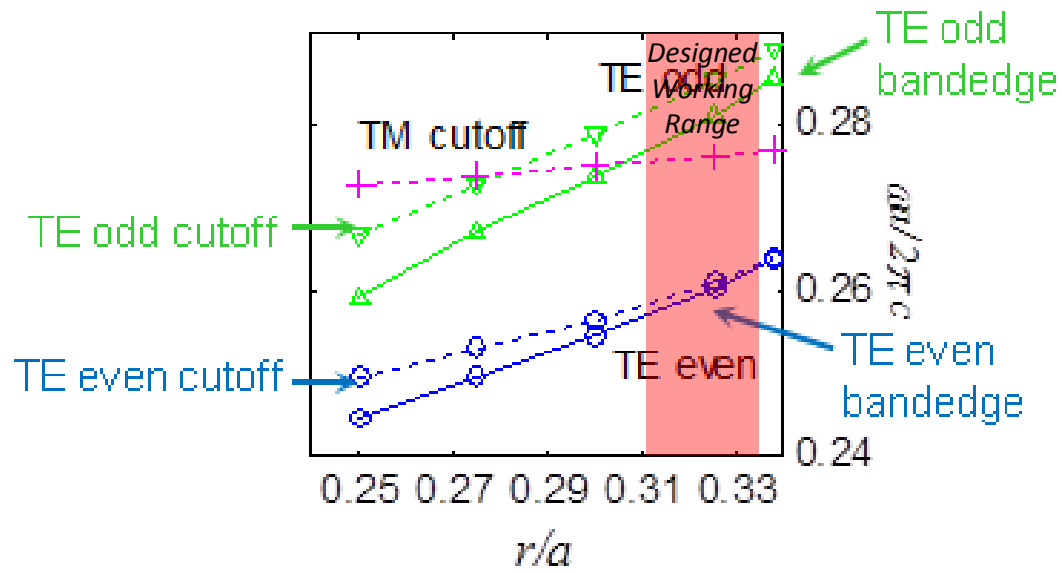
Fig. 3-2. Variation of the photonic bandedge and cutoff of even (blue) and odd (green) TE-like modes with hole radius. For each TE-like mode, the lower line (solid) gives the bandedge; the upper line (dashed) gives the cutoff frequency where a mode crosses the lightline. The TM cutoff is also shown. [93]
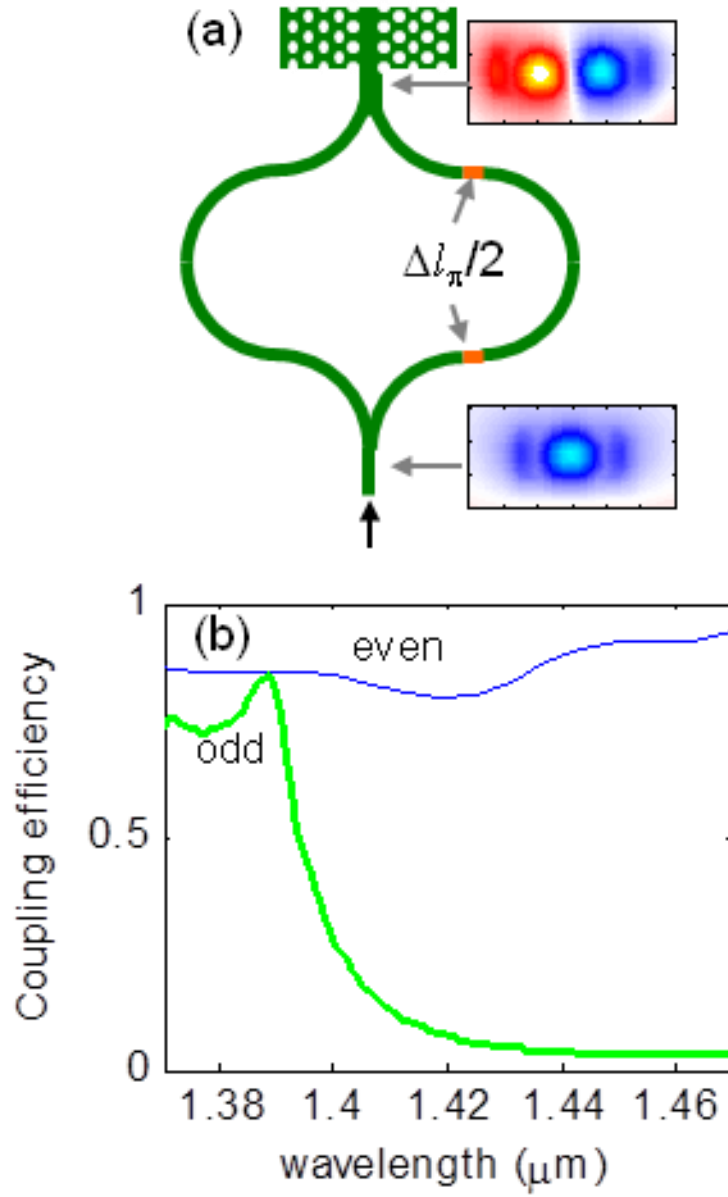
Fig. 3-3. FDTD simulation results. (a) Schematic of the Mach-Zehnder coupler

structure. The right arm has two extra waveguide segments (in orange) with a

combined length of $(\Delta l)_\pi$. The input and output E_x field profiles (cross-section)

are shown in the insets (200nm per division on axes). (b) PCW coupling

efficiency. [93]
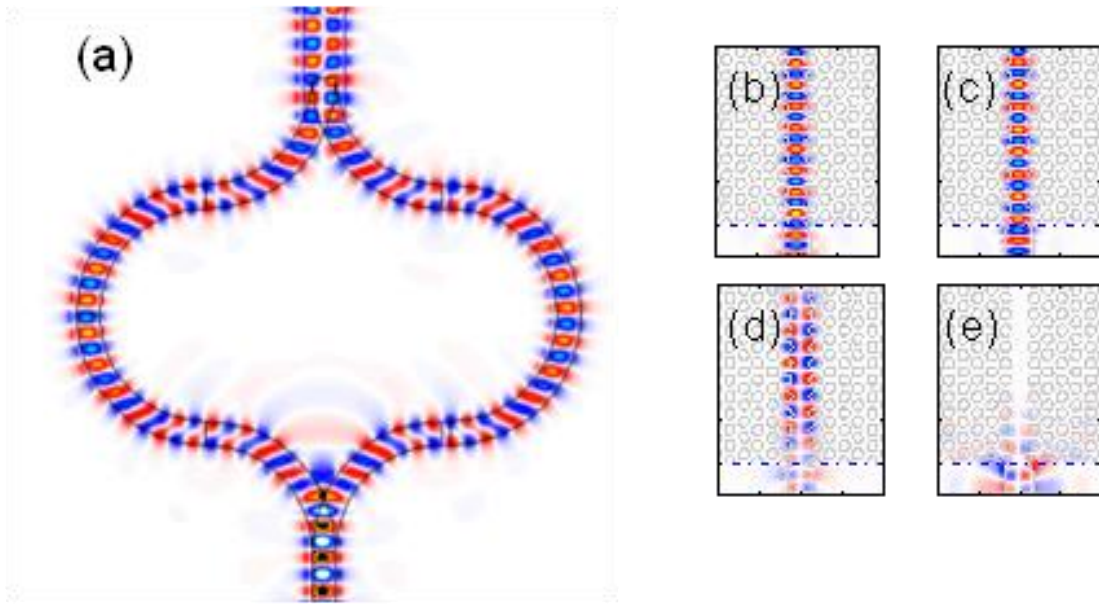
Fig. 3-4. (a) 3D FDTD simulation results of the Mach-Zehnder coupler (MZC) converting even TE-like mode to odd TE-like mode, with a smaller bend radius (2 um) for reduced simulation time and accuracy. The odd mode conversion is independent of the bend radius. (b-e) Coupled field (*Ex*) patterns as light enters from a 700 nm wide Si waveguide at the bottom of each figure and into a PCW (each division on the axes is 1 μm). (b) even at λ=1390 nm; (c) even at 1430 nm; (d) odd at 1390 nm; (e) odd at 1430 nm. [93]

Excitation of this odd PCW mode is usually deterred by the opposite symmetry of the fundamental even mode of a Si waveguide. To solve this problem, we employ a two-step approach. First, a Mach-Zehnder coupler (MZC) whose two arms have a phase difference of π is utilized to transform mode symmetry and excite an odd mode in a wide (multimode) Si wire waveguide; then this odd mode is coupled to the odd mode of the PCW. To create π phase difference in this *odd-mode* Mach-Zehnder coupler, its two arms can be designed to have a length difference of $(\Delta l)_\pi = \lambda/2n_{eff}$, where n_{eff} is the effective index of the Si waveguide. Finite difference time-domain (FDTD) simulation has been performed to confirm that such a MZC produces an odd mode in a wide output waveguide, as shown in Fig. 3-3(a). The input and output waveguide widths are 400 nm and 700 nm respectively. The coupling between the odd mode of a Si wire waveguide (700 nm wide) and that of the PCW is also simulated. Simulation results in Fig. 3-3(b) show coupling efficiencies up to ~ 84% (~0.75dB) for the odd mode. The field pattern in Fig. 3-4(d) confirms that the coupled PCW mode is an odd mode. The fundamental even mode of a Si wire waveguide couples into the PCW with inconsequential change of coupling efficiency for the spectral range in Fig. 3-3(b). The field pattern in Fig. 3-4(b) indicates that the coupled mode has even symmetry. Indeed, this mode is an even TE-like mode above the lightline. The E_x field has been shown in Fig. 3-3(a) for direct comparison with the modes of the conventional Si waveguide, whose TE-modes are commonly visualized by E_x (note E_x and H_z have the same symmetry with respect to x). Figure 3-4(c), (d) shows the field pattern of even and odd TE mode, respectively, at 1430 nm, which confirms there is no TE odd mode at 1430 nm wavelength.

3.3 Fabrication

The photonic crystal waveguide structure is fabricated on a SOI wafer with a 2 μm buried oxide layer and a 260 nm top Si layer according to the parameters used in Fig. 3-1(a). We begin the fabrication process by spinning on a positive e-beam lithography resist, ZEP 520A diluted in Anisole in the volume ratio of 1:1. After spinning at 4000 RPM for 45 seconds and baked at 180 ℃ for 3 mins, the final thickness of the resist is about 100 nm. Then the structure is patterned by a JEOL JBX-6300FS high-resolution e-beam lithography system, operating at 100 keV. After exposure, the resist is developed in Hexyl Acetate for 90 seconds, followed by rinse in Isopropanol for 45 seconds. After blown dry, the pattern is transferred to the Si layer by an Oxford Plasmalab 100 ICP etcher. The fabrication is done after removing the residual resist in 1165 remover heated at 85 ℃. The flow chart of fabrication is shown in Fig. 3-5.

Figure 3-6 is a scanning electron microscope (SEM) image of the fabricated structure. Two MZCs with a 10 μm bending radius are connected through 700 nm-wide Si waveguides of 1 μm lengths to both ends of the PCW.
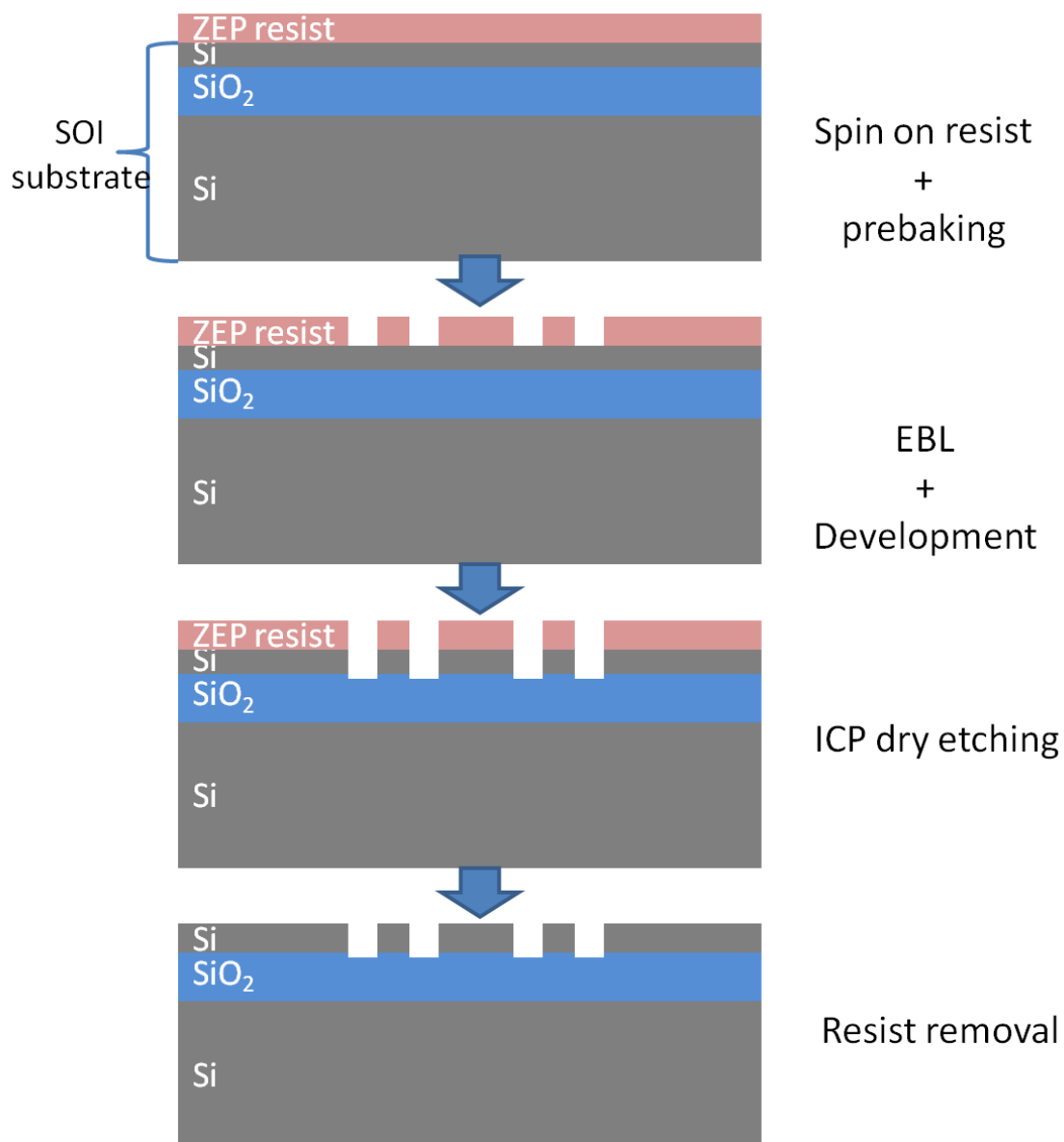
Fig. 3-5. Fabrication process flow chart.
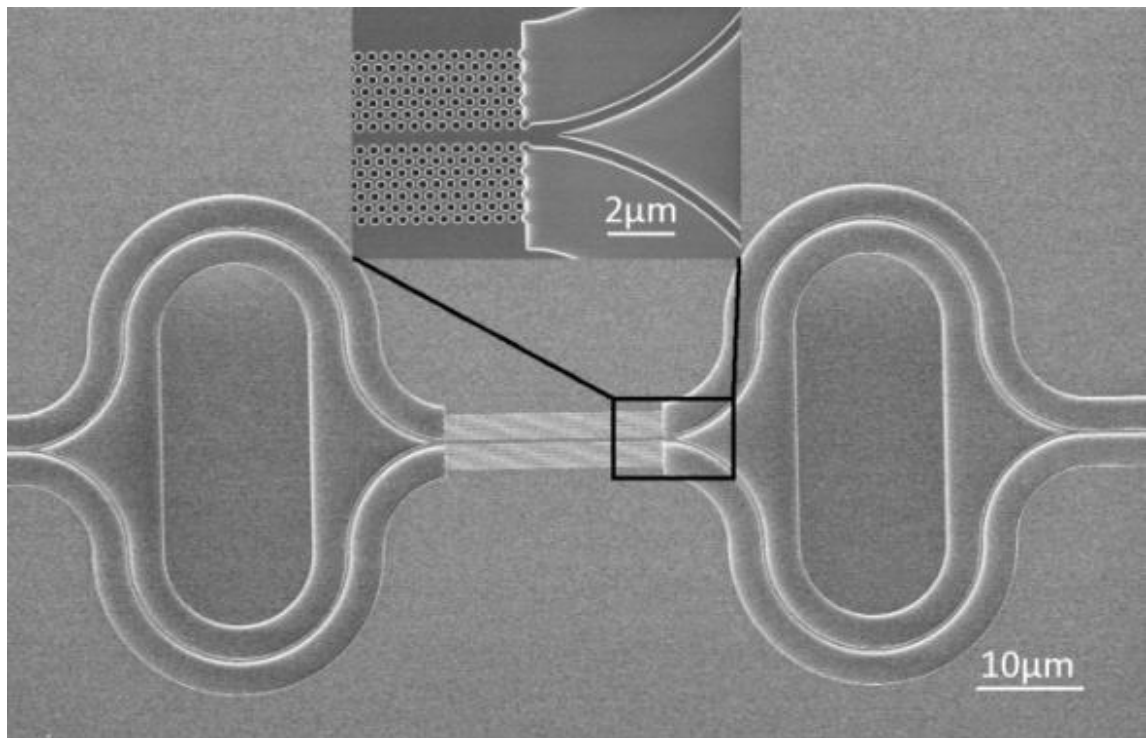
Fig. 3-6. SEM image of a PCW with odd-mode Mach-Zehnder couplers. Inset:

close-up view of the coupling region at one end of the PCW. [93]

3.4 Optical characterization results

To measure transmission spectra, light from a super-luminescent LED with a spectral range of about 80 nm is coupled to the TE mode of Si access waveguides (tapered to 4 μm at chip edges) via lensed fibers. A polarizer is used at the output end to block TM polarization. Figure 3-7 is the diagram showing our optical setup for the measurement.

The PCW insertion loss is measured with reference to a Si wire waveguide. Fig. 3-8(a) shows the spectrum of a PCW with odd-mode MZCs. A substantial transmission bandwidth is observed, approximately 22 nm at 10 dB below the peak. The contrast between the transmitted mode and background is >20 dB. The peak insertion loss is about −4 dB. Separate measurements of a reference device, which has the PCW been replaced by conventional Si wire waveguide with same length, show that each Mach-Zehnder coupler contributes ~1 dB. Thus the loss due to the PCW is estimated ~2 dB. For comparison, the spectrum of a directly coupled PCW without MZCs is shown in Fig. 3-8(b). The transmission is due to the leaky even TE-like mode as simulated in Fig. 3-4(b). By saying leaky even TE-like mode, we mean at the wavelength around 1390 nm, the even TE-like mode is above the lightline. So the even TE-like mode will meet high loss, as the light radiates into the air. But as the length of the PCW is short, after propagation through the PCW, the even TE-like mode does degrade significantly. Figure 3-8(b) also shows the PCW transmission with Mach-Zehnder couplers whose two arms have a length difference Δl deliberately designed to be 50% greater than $(\Delta l)_\pi$. Such a *mixed-mode* Mach-Zehnder coupler offers a symmetry configuration that can excite a mixture of even and odd modes according to $I_\pm \propto (1/2)[1 \pm \cos(2\pi n_{\mathrm{eff}} \Delta l / \lambda)]$. As such, the background transmission due to the even mode rises. In the odd mode band, the mixed-mode spectrum oscillates strongly due to the beating of two modes. Figs. 3-8 (a)-(b) illustrate that distinctive spectral signatures can be observed with
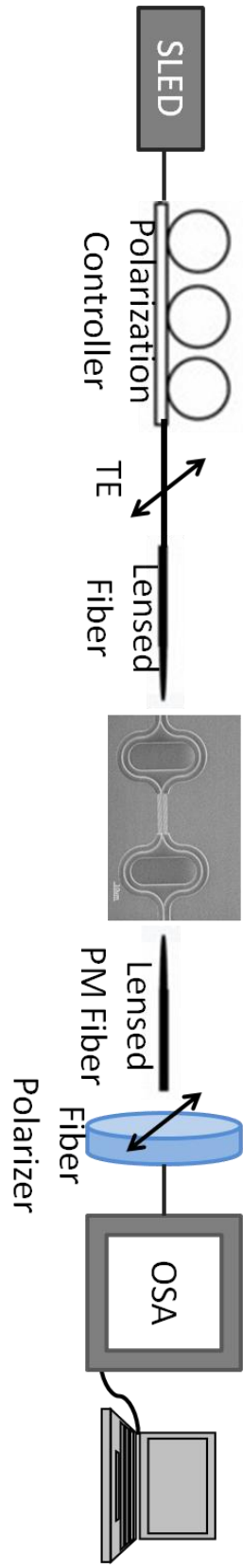
Fig. 3-7. Diagram of the optical measurement setup.
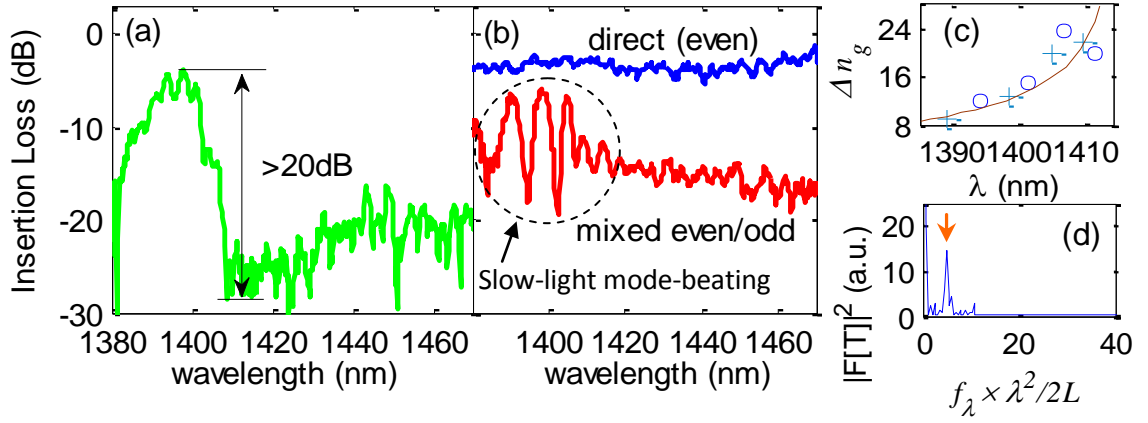
Fig. 3-8. Transmission spectra for 20 µm long PCWs: (a) with odd-mode MZCs; (b) direct transmission without MZC, and transmission with mixed-mode MZCs. (c) Δn_g obtained from the mixed-mode spectrum; the solid line delineates the trend. (d) Fourier transform of the transmission spectrum of another directly coupled PCW (the peak position gives $n_{g,even}$). [93]

controlled excitation symmetries.

The mode-beating pattern of the mixed-mode spectrum contains important information of the odd mode. The beating period is related to the group indices of even and odd modes through $\Delta\lambda = \lambda^2/(n_{g,odd} - n_{g,even})L$, where L is the PCW length (see the appendix at the end of this chapter for the derivation of this formula). Simulation indicates that $n_{g,even}$ is virtually a constant (~5) in the odd mode band. Thus the chirped beating periods are due to the dispersion of $n_{g,odd}$. We have calculated $\Delta n_g = n_{g,odd} - n_{g,even}$ from the mixed-mode spectrum and plotted it in Fig. 3-8(c). The peak-spacing and valley-spacing of the spectrum give two sets of Δn_g, data, plotted by circles and crosses respectively. They agree with each other as expected. Note that the Δn_g value obtained from two adjacent peaks (valleys) is assigned to the mid-point wavelength in-between. Further, $n_{g,even}$=4.9 is obtained in Fig. 3-8(d) through the Fourier transform [86] of the transmission spectrum of another directly coupled PCW with more obvious spectral ripples. Note that the Fourier frequency f_λ is just the inverse of the spectral oscillation period $\delta\lambda$, thus $n_{g,even}=f_\lambda \times \lambda^2/2L$. Based on Fig. 3-8(c)-(d), we find $n_{g,odd}=\Delta n_g + n_{g,even}$ in the range of 14~29. Note that the F-P oscillation amplitude in Fig. 3-8(a) is relatively weak. In contrast, the mode-beating amplitude of the mixed-mode spectrum in Fig. 3-8(b) is much higher and more robust against noise, which facilitates the evaluation of $n_{g,odd}$. Also note that in Fig. 3-8(a), the background transmission increases discernibly beyond 1430 nm due to the dispersive effect in the odd-mode MZC, which modifies the phase shift difference between the two arms as λ deviates far from the designed value (1390 nm). The TM-like mode (guided for λ>1.45 µm) may also contribute to the background at long wavelengths. However, these effects are much weaker for 1380~1415 nm.

Although this work focuses on PCWs on a SOI chip, the Mach-Zehnder coupler and the mode-beating based $n_{g,odd}$ measurement method can be adapted to the cases of air-bridge or

oxide-covered PCWs, and coupled-cavity PCWs, where interesting anomalous propagation related to an odd mode has been observed [87]. It would be interesting also to explore refined design to optimize the bandwidth and the slow-down of light together for this odd mode. Detailed discussion of these possibilities is beyond the scope of this work. The odd mode wavelength can also be shifted to ~1550 nm or other values (depending on specific applications) by changing the lattice constant. In a SOI PCW, there is some coupling between the TE-like guided modes and the TM-like photonic crystal bulk modes due to asymmetric top/bottom claddings. Prior work on the even mode has demonstrated that reducing n_g can reduce the loss due to such coupling [72]. This odd mode has a much lower n_g~14 than the normal even mode (n_g~50) below the lightline. This helps to reduce the coupling to the TM-like bulk modes. For many PCW devices operating at a short length <80 μm [76, 77], the propagation loss of the odd mode is expected to be reasonable. Lastly, the understanding of the slow light and mode-beating characteristics of this odd mode, and the controlled excitation and $n_{g,odd}$ characterization schemes developed here can facilitate the development of mode-symmetry based novel devices, such as one-way waveguides that involve active transition and passive conversion between even and odd modes [79]. Slow light can help reduce device interaction length. Note that previously demonstrated conventional-waveguide mode converters employed branching waveguides [88, 89] or multimode interference couplers [90]. Photonic crystal based mode converters have also been designed [91]. Here, the odd-mode Mach-Zehnder coupler is focused on transforming mode symmetry to attain high purity odd-mode; and the mixed-mode MZC offers a symmetry configuration for coherent mixing of even and odd modes, which enables $n_{g,odd}$ measurement through slow-light mode beating. As a side note, beating between two degenerate modes in a periodically patterned micro-

ring resonator has recently been observed, but the resonant wavelength spacing is not affected by beating [92].

3.5 Conclusions

We have experimentally demonstrated the control of excitation symmetry for an odd TE-like mode in a PCW. An odd-mode Mach-Zehnder coupler is utilized to selectively excite the odd mode with a contrast >20 dB over the background. Assisted by a mixed-mode MZC, slow-light mode beating is observed and is utilized to measure the group index of this odd mode.

Appendix: Derivation of the mode beating equation:

At the wavelengths of the spectrum peaks, the even and odd modes have phase difference *2mπ*, *m* is a constant, after traveling through the length *L* of the PCW. (Derivation for the spectrum valleys case is similar.)

$$L \cdot n_{g,odd} - L \cdot n_{g,even} = m\lambda$$

At the next peak wavelength:

$$L \cdot n_{g,odd} - L \cdot n_{g,even} = (m-1)(\lambda + \Delta\lambda)$$

Eliminate the *m*: $L \cdot n_{g,odd} - L \cdot n_{g,even} = [(L \cdot n_{g,odd} - L \cdot n_{g,even})/\lambda - 1](\lambda + \Delta\lambda)$

$$= L \cdot n_{g,odd} - L \cdot n_{g,even} + (L \cdot n_{g,odd} - L \cdot n_{g,even})\Delta\lambda/\lambda - \lambda - \Delta\lambda$$

So: $\quad (L \cdot n_{g,odd} - L \cdot n_{g,even})\Delta\lambda/\lambda = \lambda + \Delta\lambda$

$$(L \cdot n_{g,odd} - L \cdot n_{g,even})\Delta\lambda = \lambda^2 + \lambda\Delta\lambda \approx \lambda^2$$

$$n_{g,odd} - n_{g,even} = \lambda^2/L\Delta\lambda$$

Same as: $\quad \Delta\lambda = \lambda^2/(n_{g,odd} - n_{g,even})L$

Chapter 4. Interband scattering in a slow light photonic crystal waveguide (PCW) under electro-optic tuning

4.1 Introduction

Photonic crystal waveguides (PCWs) in Si have potential for CMOS-compatible on-chip optical isolators that allow propagation of light in one direction but not the other. By comparison, magneto-optical isolators are not CMOS compatible. A non-magnetic PCW technique is to employ an indirect photonic transition between two modes (e.g. even and odd modes) in PCWs, following the principle that has been investigated for Si rib waveguides with chip-scale interaction lengths of ~1cm [94, 95]. An RF-modulated even mode is converted to an odd mode through indirect interband transition after traveling forward in the PCW for a certain length, and that odd mode is filtered out at the end, blocking transmission; but in the reverse direction, the effective wave vector of the RF traveling-wave modulation does not match the wave vector difference between even and odd modes (for the reverse-propagation dispersion-relation branch). Therefore, the even-to-odd transition/conversion is weak and the even mode propagates with low loss in that direction. However, there exists another mechanism for mode conversion: inter-mode (interband) scattering due to structure imperfections. Such scattering is bi-directional and may possibly degrade the isolation. The present paper investigates interband scattering in electro-optically tuned PCW structures, and explores its impact on the performance of a PCW-based optical isolator. A potential remedy is described.

Photonic crystal waveguides have important applications in optical communications and signal processing due to their capabilities of modifying light propagation and

dispersion characteristics. Particularly, light can be slowed down in a PCW. This enhances light-matter interaction and leads to significant reduction of interaction length for optical modulators and switches [96-99] and other electro-optic devices (including aforementioned isolators based on photonic transition). Most PCW research has been focused on an even mode with the TE-like polarization. Recently, odd modes in Si-based conventional waveguides aroused interest for their potential important applications in CMOS-compatible one-way waveguides [94, 95]. A Si-based PCW also has such an odd mode. While the passive properties of this odd mode have been experimentally studied in a few reports [100, 101], the transmission characteristics under electro-optic tuning have not been reported. Knowledge of such active properties is important for making one-way waveguides based on electro-optically induced interband indirect photonic transition. Here we report the evolution of the PCW transmission spectrum under electro-optic tuning due to interband scattering in the spectral range of the odd mode.

A decrease of TE transmission in the odd mode band has been observed in a passive photonic crystal waveguide [100]. For a PCW fabricated under good conditions, small structural imperfections (e.g. small sidewall roughness of the air holes) still exist. The decrease of transmission can be attributed to structural imperfection-induced interband scattering from the even TE-like mode to the odd TE-like mode. According to the slow light scattering theory [102, 103], the loss coefficient arising from interband scattering is given by $\alpha_{i,f} \sim S_{i,f} D_i(\omega) D_f(\omega)$, where $S_{i,f}$ represents the scattering matrix element and $D_i(\omega)$ and $D_f(\omega)$ are the densities of states for the initial and final modes, respectively. Near the bandedge of the odd mode (the final mode), $D_f(\omega)$ increases significantly due to slow light [$D_f(\omega) \sim 1/v_{g,f}$, where $v_{g,f}$ is the group velocity of the final mode] and $D_i(\omega)$ is usually

almost a constant. Thus $\alpha_{i,f}$ increases and the transmission spectrum of the initial mode exhibits a notch at the odd-mode bandedge. Under carrier injection in an electro-optic device, the odd-mode bandedge shifts due to the change of refractive index, and the notch position will shift accordingly. Note that the above analysis is applicable to any initial mode, which can be the even TE-like mode as studied in Ref. [100] or the TM-like mode in the case of a PCW with asymmetric top/bottom cladding as discussed below. Note that understanding of the PCW TM-mode characteristics is of interest for optical isolators as it would be useful to have isolation for the TM mode as well.
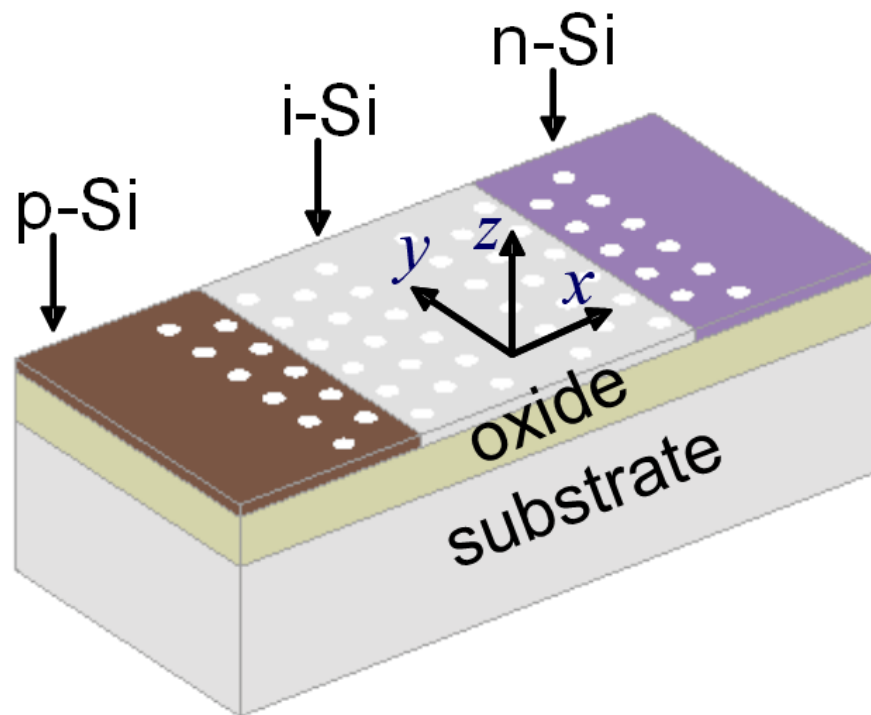
Fig. 4-1. Schematic drawing of the Photonic Crystal Waveguide structure.

(not drawn to scale) [115]
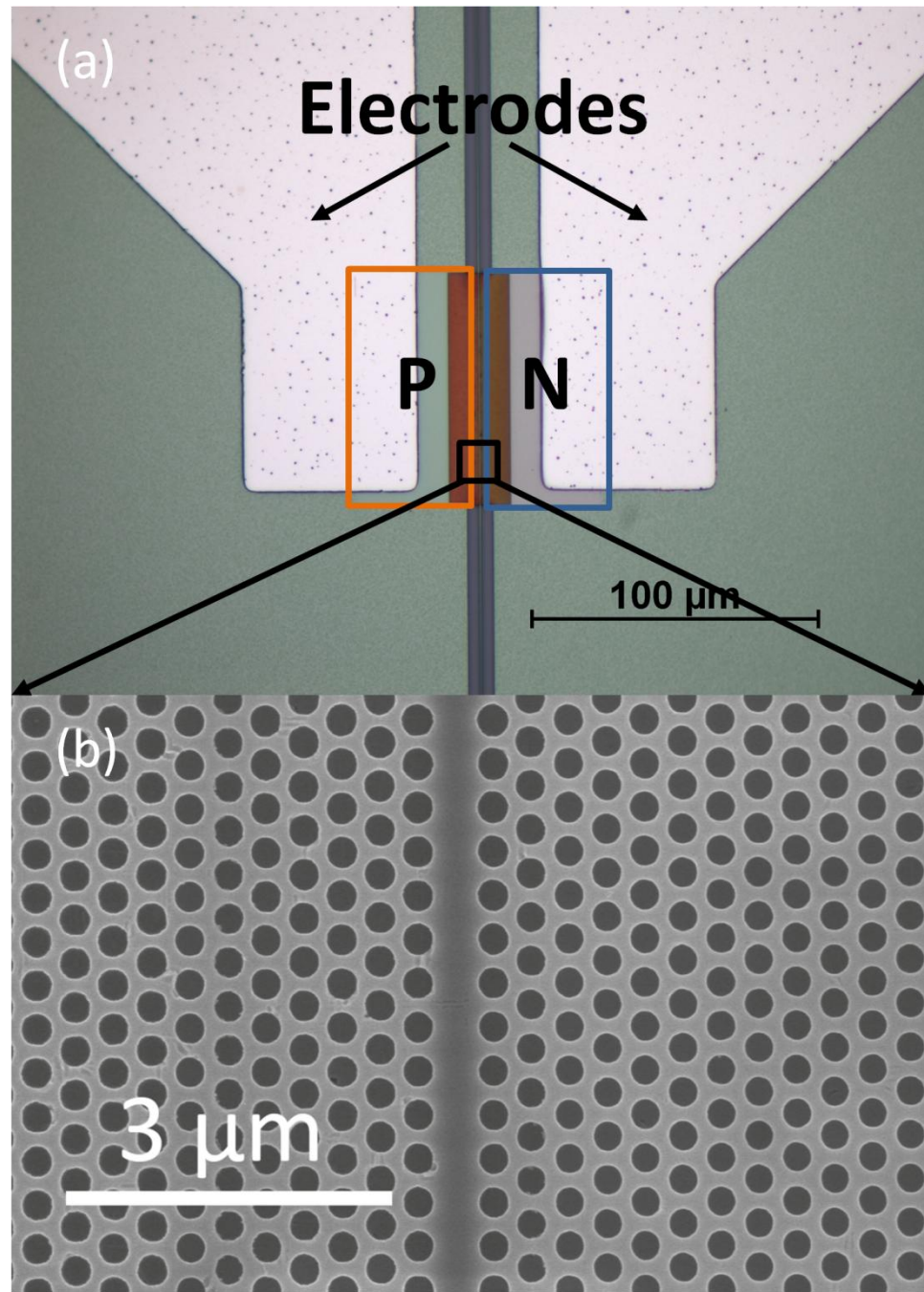
Fig. 4-2. (a) Optical image of the overall structure with p and n regions outlined by color frames; (b) SEM micrograph of the photonic crystal waveguide. [115]

4.2 Structure design and simulation

Consider a PCW formed on a silicon-on-insulator (SOI) wafer with a 260-nm-thick top Si layer, as shown in Fig. 4-1. The line defect PCW was formed in a hexagonal lattice with a lattice constant of 400 nm and an air hole diameter of 240 nm. Using the plane wave expansion method [101], the photonic band diagram is calculated and shown as solid lines in Fig. 4-3(a). The mode profiles in Fig. 4-3(b) show that the modes have imperfect vertical symmetry, due to the asymmetric air/SiO_2 top/bottom cladding. Note that the TM-like mode also has odd x-symmetry in the odd-mode wavelength range. Thus the interband scattering from the TM-like mode to the odd TE-like mode is not prohibited by symmetry. The cutoff indicates the frequency at which a mode crosses the lightline. As the hole radius increases, both the cutoff frequency of the TM-like mode and the bandedge of the odd TE-like mode move up. However, the odd-mode bandedge moves up faster than the TM cutoff. For too large of an r (e.g. $r=0.33a$), the TM cutoff will be substantially below the odd mode. As such, the TM mode transmission will be fairly low in the frequency range of the odd mode (as the TM mode is above the lightline), and the detection of interband scattering becomes difficult. For too small of an r (*e.g.* $r=0.27a$), the odd-mode and TM-like mode will cross each other, which will create a mini stop gap due to anti-crossing [104]. Because this mini-gap is usually very close to the odd mode bandedge, it complicates the observation of the bandedge shift. In this work, we have chosen $r=0.3a$ such that the TM cutoff is above the odd mode bandedge and the crossing point of these two modes is sufficiently above the lightline. Under this condition, the two modes will share a common frequency band below the lightline, yet they do not cross each other directly below the lightline. The TM-like mode can be scattered into the odd

mode due to the structural imperfection. To model electro-optic tuning of the odd-mode bandedge, the carrier injection process in a Si *pin* diode structure was simulated using Medici, an electronic device simulator. For p and n regions doped to $N_a=1\times10^{20}\text{cm}^{-3}$ and $N_d=5\times10^{19}\text{cm}^{-3}$ separated by a 2µm wide *i*-region, the calculated *i*-region carrier concentrations at various bias levels are shown in Fig. 4-4. The refractive index change can be calculated according to the electro-optic coefficient of Si [105]. The band structure under carrier injection at 3V bias is then calculated readily [106-108] based on the changed refractive index and is plotted as dotted curves in Fig. 2(a). The odd-mode bandedge shift is on the order of 10nm for 3V forward bias, which should be relatively easily observed. Based on the bandedge shift ($\Delta\lambda$) in Fig. 4-3(a), the odd-mode overlap factor with Si [106-108] can be obtained $\sigma=(\Delta\lambda/\lambda)/(\Delta n/n)$ ~0.9. Note that the TM-mode has a linear dispersion relation in the wavelength range of the odd mode. Hence its own transmission is featureless (i.e. flat) in this spectral range (and no wavelength shift would be visible) if interband scattering is absent.
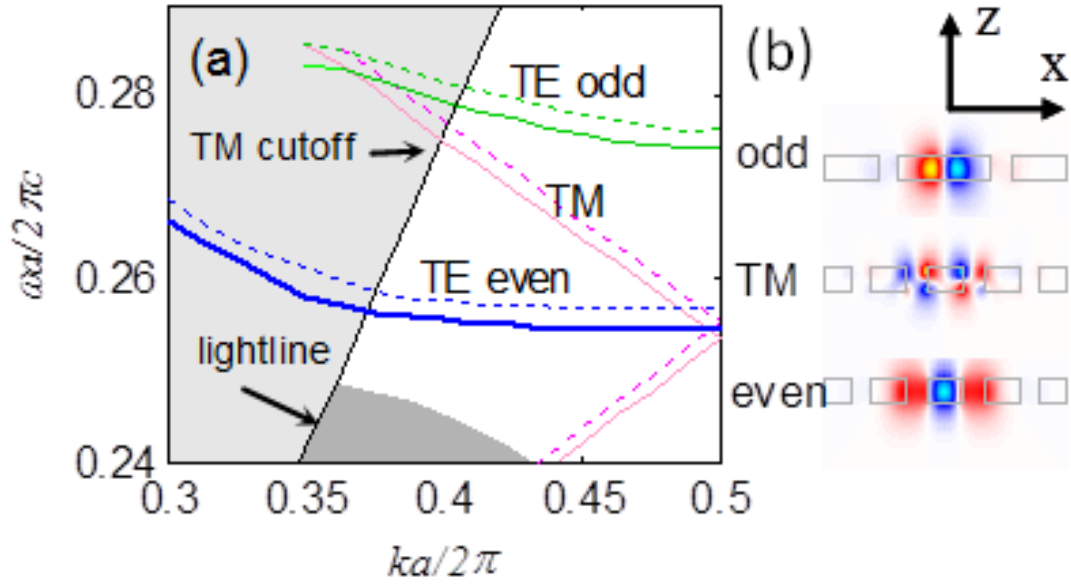
Fig. 4-3. Simulation results: (a) photonic band diagram for *r*/*a*=0.3 for original (solid curves) and 3V biased (dotted curves) structures; (b) H_z field profiles (at $k=\pi/a$) in the x-z plane at a y-section where the field peak of the mode appears. The PCW structure is sketched by grey lines. [115]
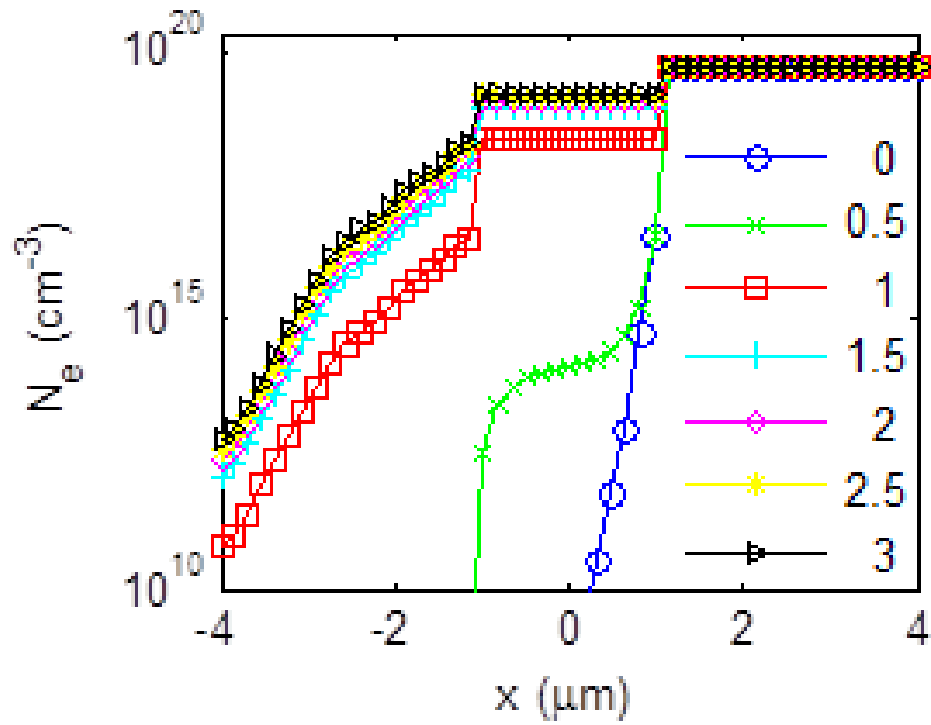
Fig. 4-4. Electron concentration at various forward bias levels obtained from Medici. [115]

4.3 Fabrication and Characterization

The PCW structure was fabricated according to the parameters of the structure simulated in Fig. 4-3. The optical waveguide layer was patterned on a SOI wafer by electron-beam lithography and followed by inductively coupled plasma dry etching. P and N regions were defined using photolithography and were doped by implantations sequentially. Piranha cleaning was done after implantation. The contact windows were opened alongside the PCW by a third photolithography process, and titanium/aluminum alloy electrodes were deposited by e-beam evaporation, followed by a liftoff process and rapid thermal annealing. The contact resistances of the p and n pads were about 30 Ω and 25 Ω, respectively, which were obtained based on testing Si resistors with same contact pads fabricated on the chip. The total device length including access Si wire waveguides is about 3.5mm.

The fabrication process flow chart is shown in Fig. 4-5.

After fabrication, the sample was tested using the setup shown in Fig. 4-6. It is similar to the setup we saw in the previous chapter, but we are measuring the optical spectrum for the TM like mode, instead of the TE like mode. And various DC bias voltages were applied on the PN diode.

EBL + ICP Si etching

Photolithography + P⁺ implantation

Photolithography + N⁺ implantation

1000°C RTA + Piranha clean

Photolithography + Metal deposition + liftoff

400°C RTA
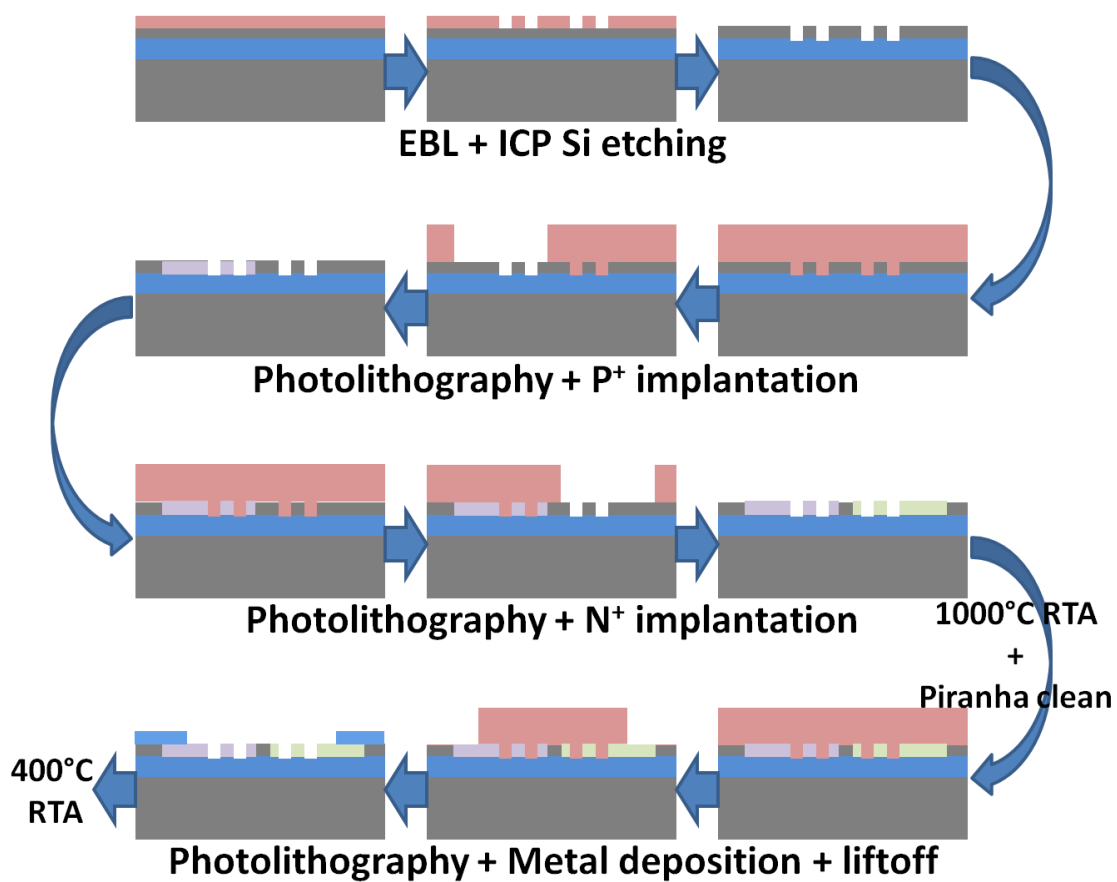
Fig. 4-5. Fabrication process flow chart.
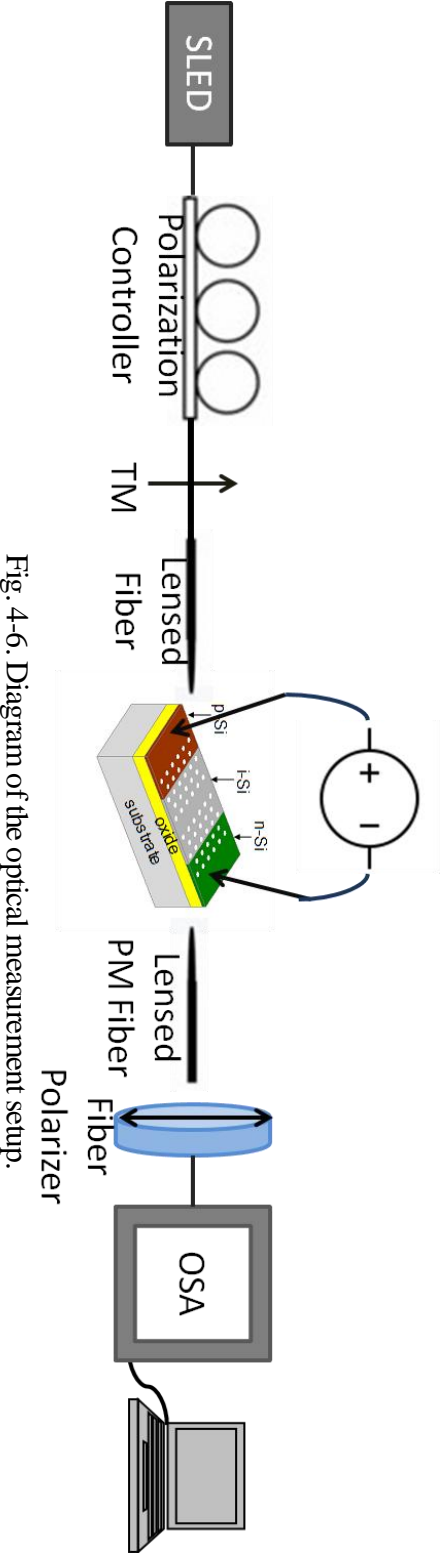
Fig. 4-6. Diagram of the optical measurement setup.
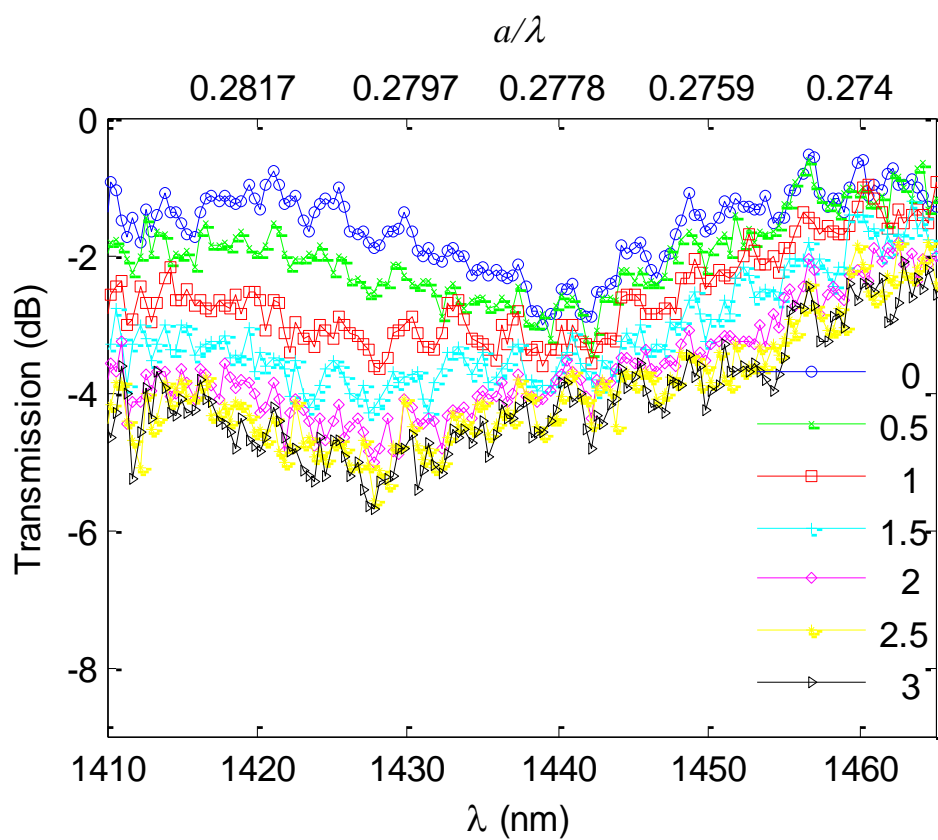
Fig. 4-7. Spectra of the pin diode-embedded PCW under various bias levels. [115]

The spectral transmission characteristics of the fabricated sample were measured at various bias levels as shown in Fig. 4-7. A broadband superluminescent LED with a useful spectral range of about 50nm was used as the light source. Polarization-maintaining lensed fibers were used to couple light into the TM polarization of a Si wire waveguide. Then light is transported by the Si wire waveguide to the 80μm-long PCW. Light exiting the PCW is delivered by another Si wire waveguide to the output lensed fiber. The transmission in Fig. 4-7 is normalized by the LED spectrum plus a fixed reference loss value of a reference Si wire waveguide. Compared to normalization by the spectrum of a reference wire waveguide, this approach avoids introducing extra spectral noise of the reference wire waveguide. This might make the peak insertion loss less precise—but we are primarily interested in the wavelength shift and lower noise here. As expected, a spectral valley appears in the odd-mode band due to interband scattering. As the bias increases, the spectral valley shifts towards shorter wavelengths. Due to noise, the spectrum is not smooth. Instead of a clear single minimum point on the spectrum, multiple local minima of similar depths may be present in the neighborhood of the spectral valley. It is difficult to assign a single spectral notch precisely. Here we employ a statistical approach to determining the spectral notch wavelength. For the spectrum at a given bias, the wavelengths of the n lowest local minima of the transmission spectrum were recorded; then the mean value and the variance of this set of wavelengths were calculated statistically. The results for $n=3$, 4, and 5 are plotted in Fig. 4-8(a) for each bias level. Clearly, the results for various n values agree with each other fairly well and show a definite valley shift. The inset of Fig. 4-8 shows the measured I-V relation of the *pin* diode. The differential resistance under large forward bias is estimated around 118Ω.
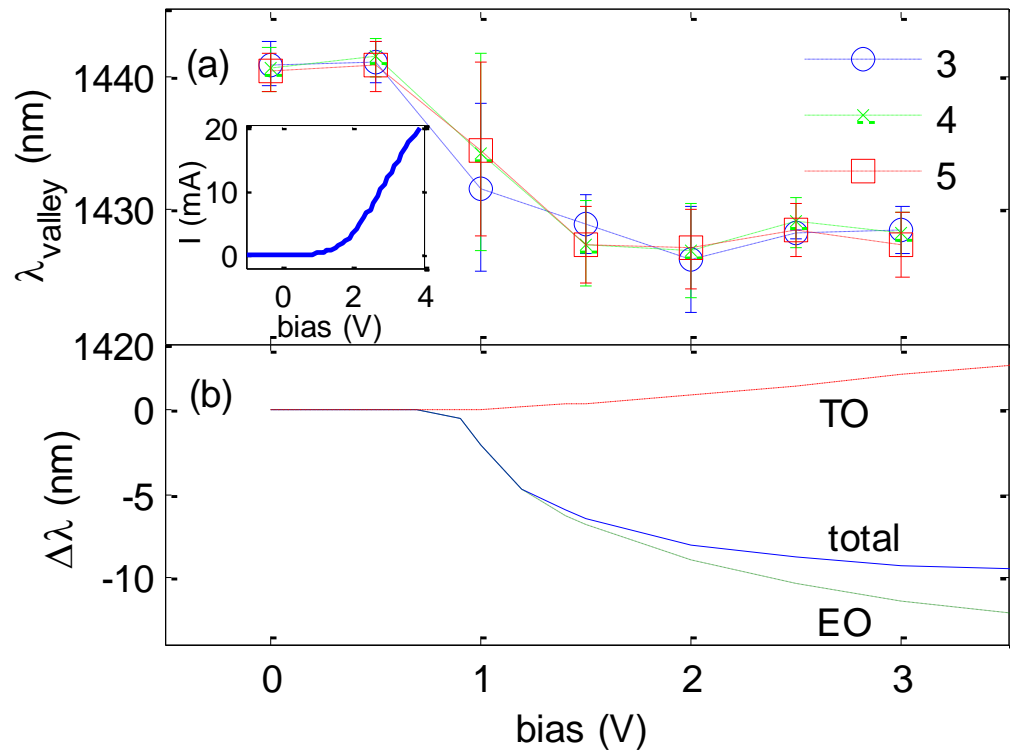
Fig. 4-8. Shift of the spectral valley wavelength vs. static forward bias. (a) experimental results based on statistics of the lowest *n* local mimima of the spectrum (*n*=3, 4, 5). Inset: I-V curve of the pin diode. (b) Simulated shift due to electro-optic (EO) and thermo-optic (TO) effects. [115]

4.4 Discussions

In Fig. 4-8(b), the band shift $\Delta\lambda$ evidently saturates at large bias. This is because the band shift is not solely determined by the electro-optic effect, but also by the thermo-optic effect accompanying the joule heating in the *pin* diode. Also, the electro-optic effect and the thermo-optic effect change the refractive index in opposite directions. The thermo-optic effect was simulated using the approach described Ref. [109]. The total temperature rise in the PCW core includes contributions from the heating in the *i*, *p* and *n* regions. The heat generated by the contact resistances had little effect on the temperature rise in the PCW core because the contacts are far from the core (~20 μm, more than three times the thermal spreading length). At low voltages (V<1.5V), the electro-optic effect dominates. As the current rises at high forward biases, the thermo-optic effect due to joule heating becomes substantial. Together, the electro-optic and thermo-optic effects shift the odd-mode band as plotted in Fig. 4-8(b). The simulation result provides a reasonable trend of the spectral shift of this odd mode.

Note that in the odd TE-like band, the even TE-like mode is far above the lightline and has substantially higher loss and worse noise. This obscures the observation of the spectral features and therefore the TM-like mode is suitable for input in the present structure instead of the TE-like mode. In addition to the coupling via structural imperfection-induced interband scattering throughout the PCW length, the TM-like mode may also couple to the odd TE-like mode at the PCW interface. Due to the asymmetric top/bottom cladding, the TM-like mode and odd TE-like mode are not perfectly orthogonal (these two modes have the same *x*-symmetry and approximately opposite *z*-symmetry, as shown in Fig. 4-3a), which causes this coupling at the PCW interface.

However, such coupling is extremely weak because the two modes have approximately opposite z-symmetry and a large group velocity mismatch (n_g<5 for the TM-like mode of a Si wire waveguide and n_g≥15 for the odd TE-like mode). FDTD simulations show that such interface coupling causes a very small loss <0.3dB per PCW interface over the entire odd-mode band. Such a weak effect was easily buried in the noise (~0.5dB in Fig. 4-7) of the spectrum. Note that at PCW interface, the coupling ratio between the TM-like mode and even TE-like mode is zero because of their opposite x-symmetry (for comparison, the interface coupling ratio between the TM-like and odd TE-like mode is <7% from FDTD simulations). However, the interband scattering between two modes of different polarizations is not prohibited/restrained by symmetry in this structure due to asymmetric top/bottom cladding (also note each mode is not purely TE or TM). This is different from the air-bridge structures [110, 111]. The even TE-like mode transmission below the light line is normal: it shows a bandedge around 1570nm but no interband scattering valley because the TM bandedge is at λ>1570nm. To launch an odd TE-like mode needs a carefully fabricated Mach-Zehnder coupler [101], which is not included in the present device. For the odd TE-like mode spectrum, it is expected that while the interband scattering from the odd TE mode to the TM mode is enhanced by $1/v_{g,odd}$ at the odd mode bandedge, this signal will be buried by the backscattering (more strongly enhanced by $1/v_{g,odd}^2$ [102, 103]) of the launched mode (odd mode). Note that backscattering and out-of-plane scattering (to radiation modes) are significant only at the bandedge of the initial mode (the launched mode) [102, 103]. In this work, we have chosen a wavelength range near the bandedge of the final mode (odd mode) and far away from the bandedge of the initial mode (TM-like mode). Thus, only the interband

scattering is enhanced, and backscattering and out-of-plane scattering are not enhanced and are much weaker than interband scattering. Despite the spectral noise, the spectral notch position due to the interband scattering can be determined statistically within 1σ of all data sets for $n=3\sim5$. This indicates that our method is independent of the number of spectral minima.

Note that optical isolators based on an indirect photonic transition can, in principle, achieve very high isolation [94]; up to 20dB difference for forward-to-backward transmission has been demonstrated in fiber-optic devices [112]. In Si-based waveguide devices, the isolation can be degraded by a variety of factors including RF impedance mismatch of the driving circuitry (which reduces the modulation/transition efficiency), the thermo-optic effect (which counteracts the electro-optic modulation and is not unidirectional), and interband scattering. Most of these secondary effects have been studied in optical modulators, therefore there is a knowledge base available for further improvement. However, the interband scattering effect is seldom studied in electro-optic devices, particularly for slow-light PCWs under electro-optic tuning. Here the notch depth due to interband scattering in Fig. 4-7 is found to be relatively small (about 2.5~3.5dB for all applied voltages) compared to ~10dB modulation depth achievable in PCW modulators with a similar interaction length [97, 113]. For the one-way waveguide (isolator) based upon an electro-optic modulation-induced photonic transition [94], this is a positive indication that the effect of electro-optic modulation would likely be substantially stronger than the undesired interband scattering.

(a) forward (ideal)

mode filter *modulated PCW* *blocked by mode-filter*

input

T

zero output

y

(b) forward (w/ scattering)

blocked by mode-filter

T S S

y

0 L_B

(c) backward (ideal)

input

y

(d) backward (w/ scattering)

blocked by mode-filter

S S

y
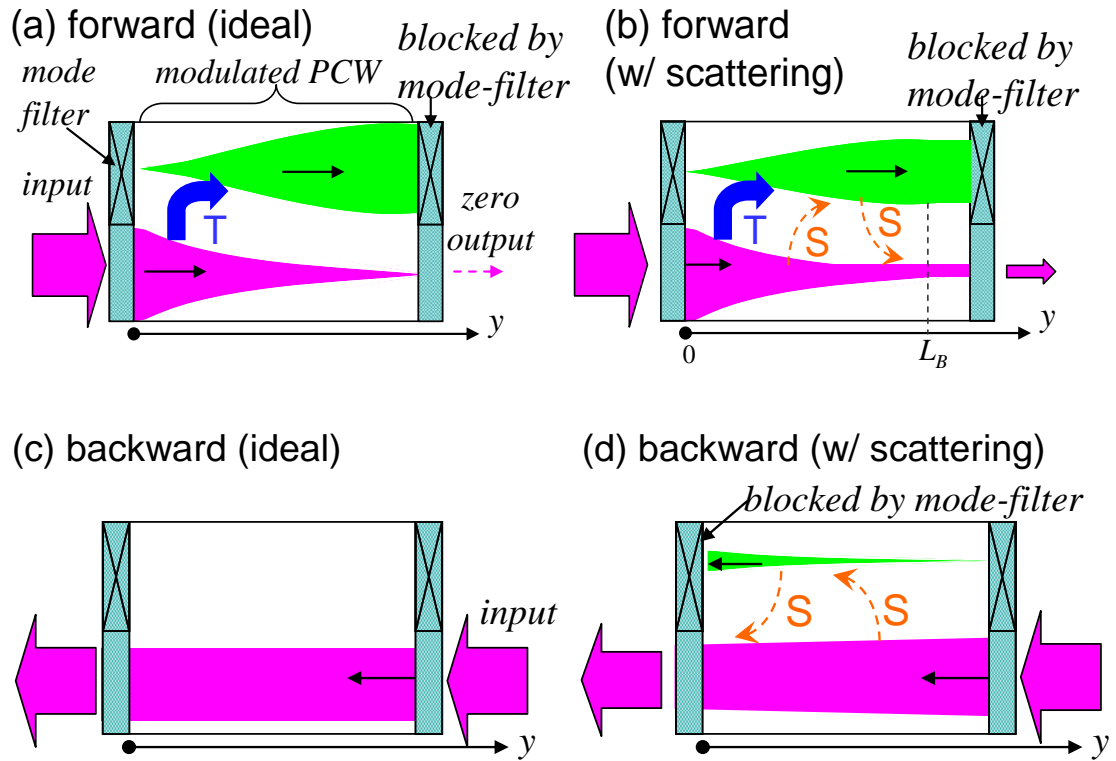
Fig. 4-9. Schematic of interband scattering effect in an optical isolator based on indirect interband transition. The launched mode (e.g. TM mode) is marked in purple, and the converted mode (odd mode) in green. The mode filters block the odd mode only. The width increase (decrease) of a beam indicates the mode intensity growth (decay). Interband transition due to E-O modulation is marked in blue (and letter "T"), interband scattering in orange (and letter "S"). [115]

For further analysis, consider an isolator composed of a modulated waveguide with a mode filter at each end [94]. For the forward path (ideal case) in Fig. 4-9(a), the launched mode (e.g. TM mode) is fully converted to a final mode (e.g. odd mode) by interband transition, and the odd mode is blocked by the mode filter. By proper design, the indirect interband transition can occur from the initial mode to the final mode ($i{\rightarrow}f$) in the forward path only (not $f{\rightarrow}i$ nor any type in the backward path) [94]. When interband scattering is included in Fig. 4-9(b), the back-and-forth scattering between the TM and odd modes results in some residual TM mode at the end. Based on the scattering coefficient formula [102, 103], one can readily see that the interband scattering loss coefficients between any two guided modes are symmetric, $\alpha_{i,f}=\alpha_{f,i}$. Assuming other losses are negligible, after a sufficiently long propagation length $y=L_B$, the interband transition and two-way scattering reach a balance: $tI_i(y)+\alpha_{i,f}I_i(y)-\alpha_{f,i}I_f(y)=0$, where t is the interband transition coefficient per unit length (in dB/cm), $I_i(y)$ and $I_f(y)$ are the intensity for the initial launched mode (TM) and converted mode (odd), respectively. Under the lossless assumption, the total intensity at $y=L_B$ satisfies $I_i(L_B)+I_f(L_B)=I_i(0)$. Thus we obtain

$$I_i(L_B)/I_i(0)=\alpha_{i,f}/(t+2\alpha_{i,f}). \qquad (1)$$

This determines the residual intensity (hence the isolation) at the output. For example, if $\alpha_{i,f}/t=3/10$, the optical isolation would be $10\log_{10}[I_i(L_B)/I_i(0)]= -7.3$dB. Fig. 4-9(b) also indicates that $I_i(y)$ and $I_f(y)$ remain constant for $y>L_B$ (after the balance between the interband transition and scattering is reached). This suggests rather than having an isolator of $2L_B$ length, two cascaded isolators of L_B each can possibly improve the isolation by two times. Here excellent mode filters are assumed in each isolator section,

otherwise the isolation improvement will be less. Note that mode filters (or passive mode converters) with >20dB mode-selectivity [101] are achievable. The primary effect of the interband scattering for the backward path, shown in Fig. 4-9(d), is some excess loss (a few dB) for the isolator. Note that free carrier absorption caused overall decrease of transmission in Fig. 4-7. The absorption affects both forward and backward propagation. For the backward propagation, it increases the device insertion loss. Also note that under modulated bias, the time average of the scattering loss spectra at varying bias levels may result in a broad valley roughly covering all spectral notches from 0V to 3V.

This work is focused on investigating the effect of interband scattering on the new isolator based on the indirect interband transition. Of course, to further demonstrate a PCW based isolator, the dispersion relations of two waveguide modes and the doping of Si need to be judiciously tailored [95] to translate the full potential of electro-optic modulation depth into high isolation and better impedance matching. Prudent junction design and higher electric driving power can also help. Detailed discussion of these techniques is beyond the scope of this work. Besides the cascading approach (one remedy) discussed above, the interband scattering effect can also be minimized by reducing structure imperfection (e.g. through tight process control in industrial-grade cleanroom facilities). An additional way to reduce interband scattering is to increase the wavelength of operation into the mid infrared range [114] by scaling up the waveguide dimensions. In that case, the structure imperfections of the present paper will have a much smaller effect.

4.5 Conclusions

In summary, the evolution of the PCW transmission spectrum in the odd mode band is studied under electro-optic tuning. The shift of the odd-mode band under carrier injection has been observed through interband scattering. The band shift is determined statistically from the measured spectrum with noise. The spectral shift was accounted for by electro-optic and thermo-optic effects. The impact of interband scattering for the isolator application is analyzed and potential remedies are discussed.

Chapter 5. Quarter wavelength resolution aluminum superlens working at 193nm DUV

5.1 Introduction

Nanopatterning is one of the key steps in fabrication of nano-scale electrical and optical devices. Some of the technologies in use are electron beam lithography (EBL), ion beam lithography (IBL), nano-imprint lithography (NIL), focused ion beam (FIB) milling, dip pen lithography and etc. However, they are facing some critical challenges such as high cost, low throughput in large scale patterning, low controllability, low accuracy, and alignment difficulties. Some foundries have state-of-art Extreme Ultraviolet (EUV) and Deep Ultraviolet (DUV) photolithography tools. But they are economically hard to access.

Since the concept of a plane perfect lens was developed by Pendry in 2000 [116], numerous superlens structures were proposed theoretically and demonstrated experimentally by different research groups [117-120]. Superlens relies on the achievement of negative index material (NIM) to enhance the evanescent wave in near field region and excite surface plasmons. A perfect NIM requires both the permittivity and permeability to be negative (ε=-1 and μ=-1), which is difficult to realize in DUV range. Fortunately, Pendry also suggested that for normal incident transverse magnetic (TM-) polarized (also called p- polarized) light, negative dielectric permittivity is sufficient to achieve superlens performance.

Researchers investigated silver (Ag) superlens structures for imaging at UV wavelengths because Pendry predicted that Ag would be a good NIM. By optimizing

superlens structural parameters (like layer thicknesses, mask layer material, and surface roughness), numerous milestones were achieved. In 2010, 30 nm half pitch grating imaging with 6 nm channel depth was realized on smooth Ag superlens devices using 380 nm wavelength illumination [118]. In 2012, 3D gray scale imaging with high aspect was also reported on an Ag superlens using 365 nm UV light [119].

In 2009, Shi et al. proposed a structure using aluminum (Al) as the top superlens material for 193 nm DUV illumination [121-122]. The very short DUV wavelengths translate into a large modulus of the lateral Surface Plasmon (SP) wave-vectors, leading to a larger absolute bandwidth of enhanced lateral wave-vectors. This helps to improve the resolution compared to superlens structures designed for visible or near UV illumination. At 193 nm, tungsten (W) has a higher imaginary part of the refractive index (n=1.3+3.02i) (compared to n=1.02+1.17i for silver or n=1.43+1.16i for gold) [123], so it can absorb incident light more effectively, which is beneficial as a mask material.

MgO has been used as a dielectric insulator layer to provide permittivity matching to a top Al superlens layer, in order to improve the performance to some degree [121]. However, after further simulation, it was found that using SiO_2 instead of MgO would not degrade the performance of the Superlens as neither of them can provide perfect index match, and MgO was eventually replaced in later designs [122]. In the current research discussion, we present promising performance results of using pure SiO_2 as the dielectric insulator with an Al top superlens layer, completely avoiding the difficulties of depositing a conformal smooth MgO permittivity matching layer.
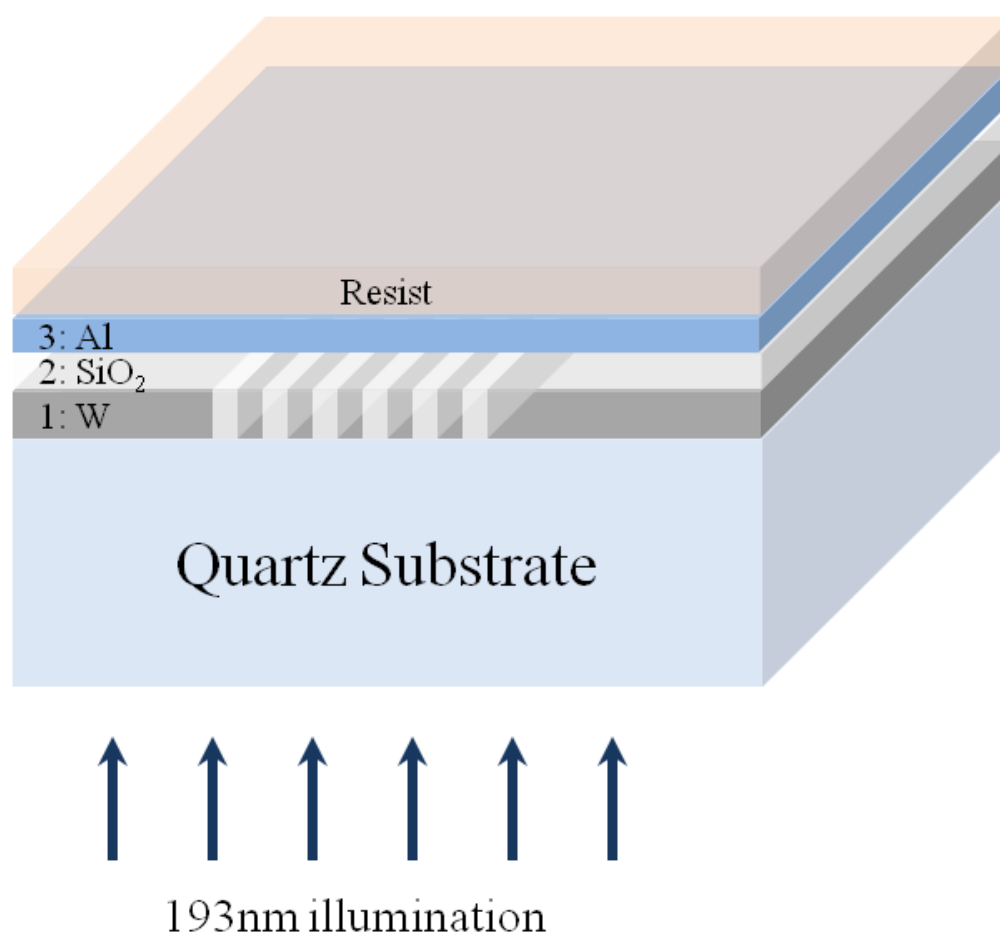
Fig. 5-1. Schematic diagram of the Al superlens working at 193 nm DUV, with W grating as the mask and SiO_2 as the dielectric insulator.

5.2 Design and fabrication

Figure 5-1 shows the device structure. A 20 nm thick W layer was initially sputtered onto a quartz substrate. Then the grating and arbitrary designs were patterned by a JEOL JBX-6300FS high-resolution e-beam lithography system, operating at 100 keV, on a 100 nm thick layer of ZEP 520 A e-beam resist. SF_6 based reactive ion etching (RIE) was applied to transfer the patterns into the W layer. Subsequently, the residual resist was removed by immerging the sample in 1165 remover at 80 ℃ for more than half hour. Figure 2(a) and 3(a) shows the scanning electron microscope (SEM) image of fabricated patterns in the W mask layer. On top of the W mask, 50 nm SiO_2 was deposited by plasma enhanced chemical vapor deposition (PECVD). Chemical mechanical polishing (CMP) was used to thin the layer down to 14~17 nm and the SiO_2 surface planarization was achieved at the same time. In the end, 13 nm Al superlens layer was sputtered on top of the SiO_2 dielectric layer. Atomic force microscope (AFM) image shows the root mean square (rms) surface roughness of 0.873 nm in a 2 μm by 2 μm area.
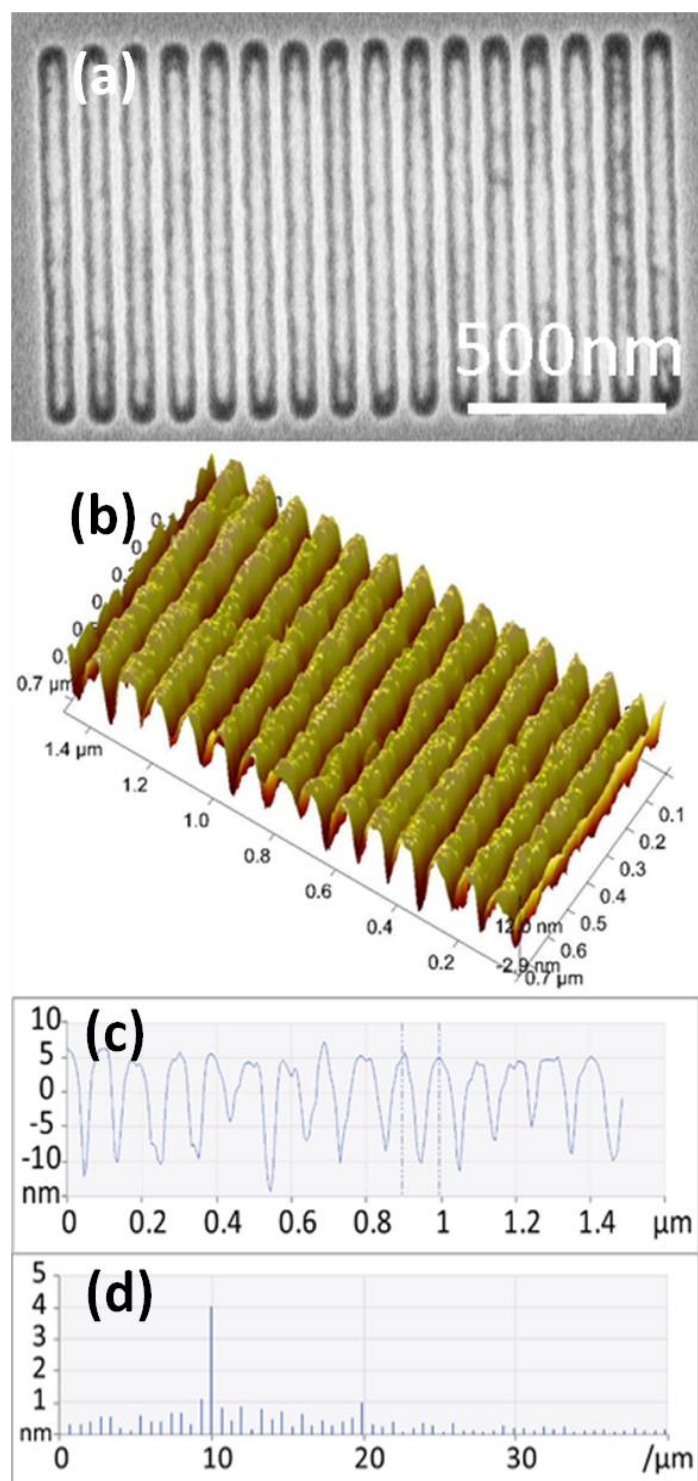
Fig. 5-2. (a) SEM image of 50 nm half-pitch grating on W layer; (b) 3D AFM image of 50 nm half pitch grating in PMMA; (c) cross section of (b); (d) Fourier analysis of (c).
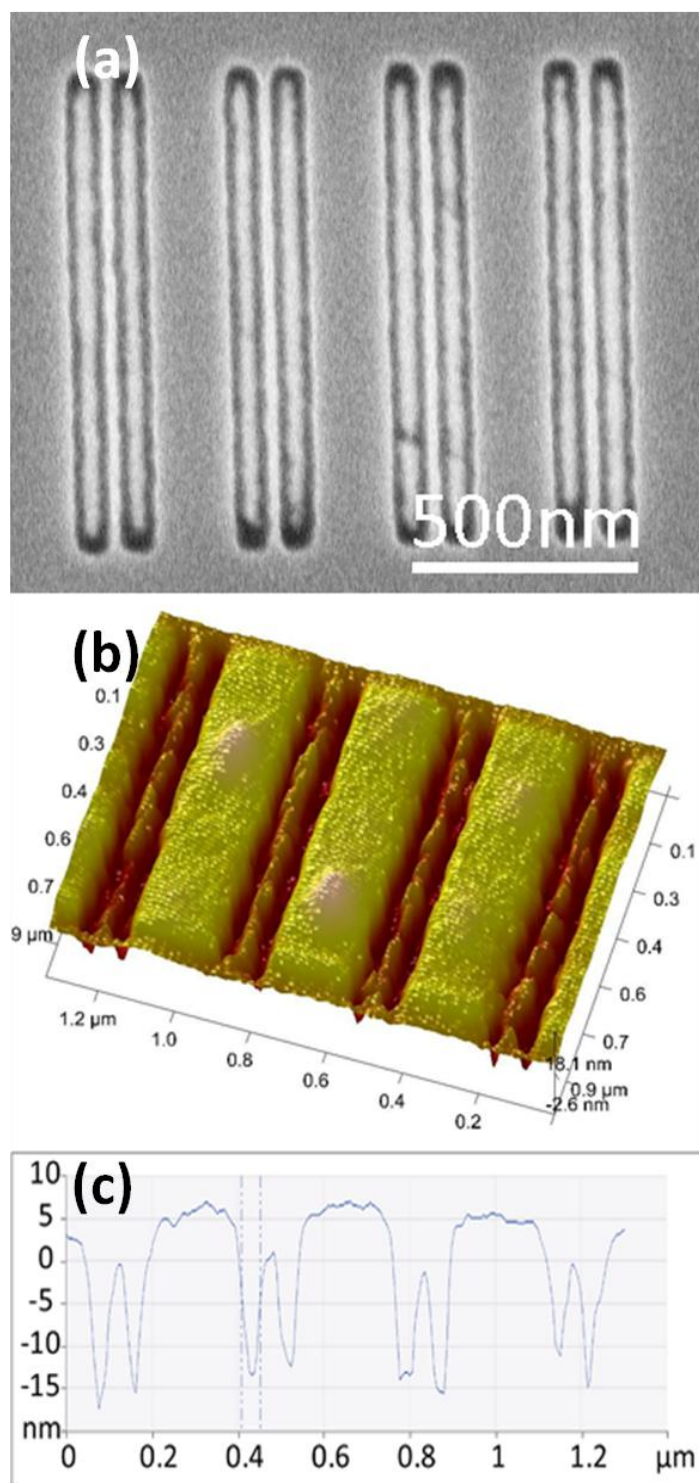
Fig. 5-3. (a) SEM image of 50 nm spacing 50 nm width double slits on W

layer; (b) 3D AFM image of 50 nm spacing 50 nm width double slits in

PMMA; (c) cross section of (b).

5.3 Characterization

To characterize the performance of our superlens samples, 20 nm PMMA resist, after diluting 495PMMA A2 with A thinner (both from MicroChem) in the ratio of 1 by 1 (diluted to 1% volume percentage), was coated on top of the superlens Al layer to record the image, followed by baking on 180 ℃ hotplate for 90s.

A low cost, non-toxic laser driven DUV lamp was used as the light source of our exposure system. After filtering, the light beam, centered at 193 nm with 15 nm bandwidth, has a light intensity about 10 mW/cm^2. Calculation shows 10min DUV exposure will provide enough dose for the PMMA resist to change property. Figure 5-4 shows the exposure setup. After exposure, the sample was immerged in the PMMA developer, 1:3 MIBK to IPA, for 30s, followed by IPA rinse for another 30s. To increase the development contrast, the developing process was operated in low temperature condition. We tried several temperatures, including 0 ℃, -2.8 ℃, -10 ℃, and -13 ℃. The best image was achieved when developing at -2.8 ℃.

The images were produced successfully. Fig. 5-2(b) is the AFM image of 50 nm half pitch grating in PMMA. The cross section profile of the grating is shown in Fig. 5-2(c). The best pattern depth we achieved is about 15 nm, when the development temperature was at -2.8 ℃. The Fourier analysis, Fig. 5-2(d), shows a clear peak at 10 μm^{-1}, corresponding to 100 nm period grating. We also exposed 50 nm spacing 50 nm width double slits pattern. The AFM image and related cross section profile are shown in Fig. 5-3(b) and Fig. 5-3(c). All these results prove that we have achieved quarter (¼) wavelength resolution by Al superlens.
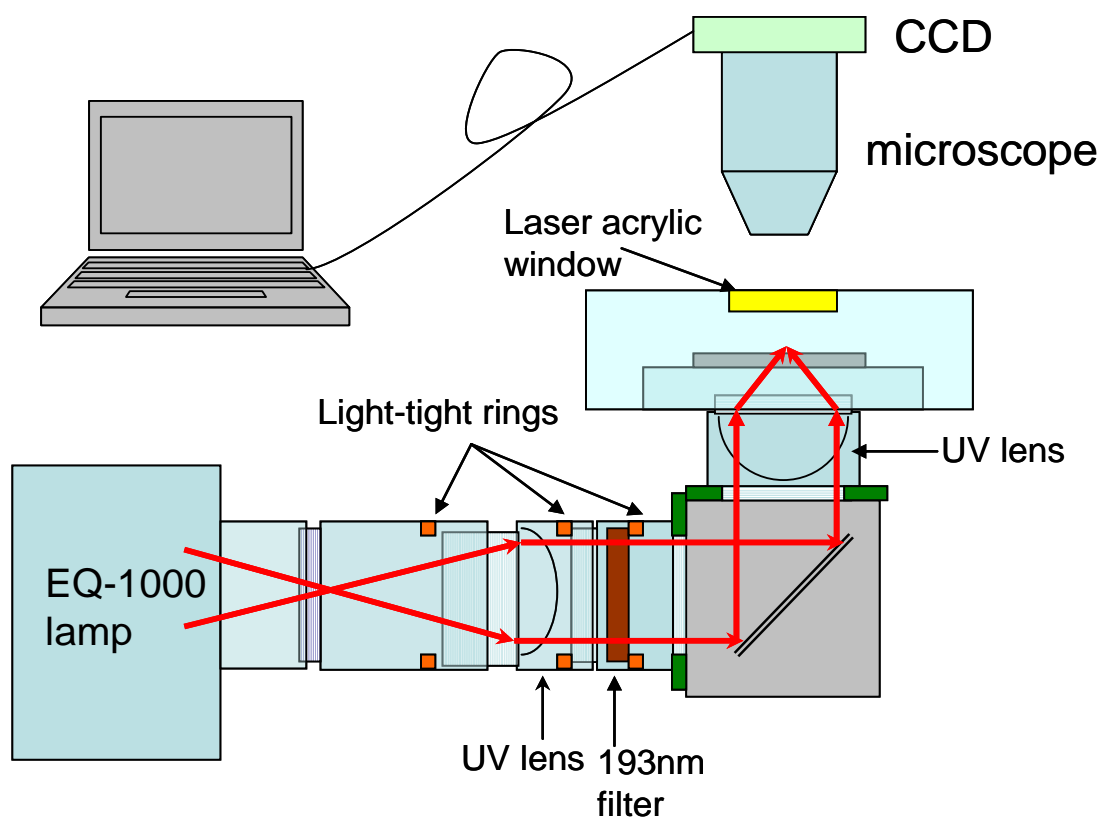
Fig. 5-4. Diagram of 193 nm DUV exposure setup. [124]

To illustrate the performance of superlens, we fabricated a control sample similar to the superlens sample, except the Al superlens layer was replaced by SiO_2 and the exposure time was reduced to 7 minutes. The results turn out that, gratings with 200 nm period (100 nm half-pitch) and above can be imaged well (Fig. 5-5). But no image is observed for the grating period smaller than 100 nm.
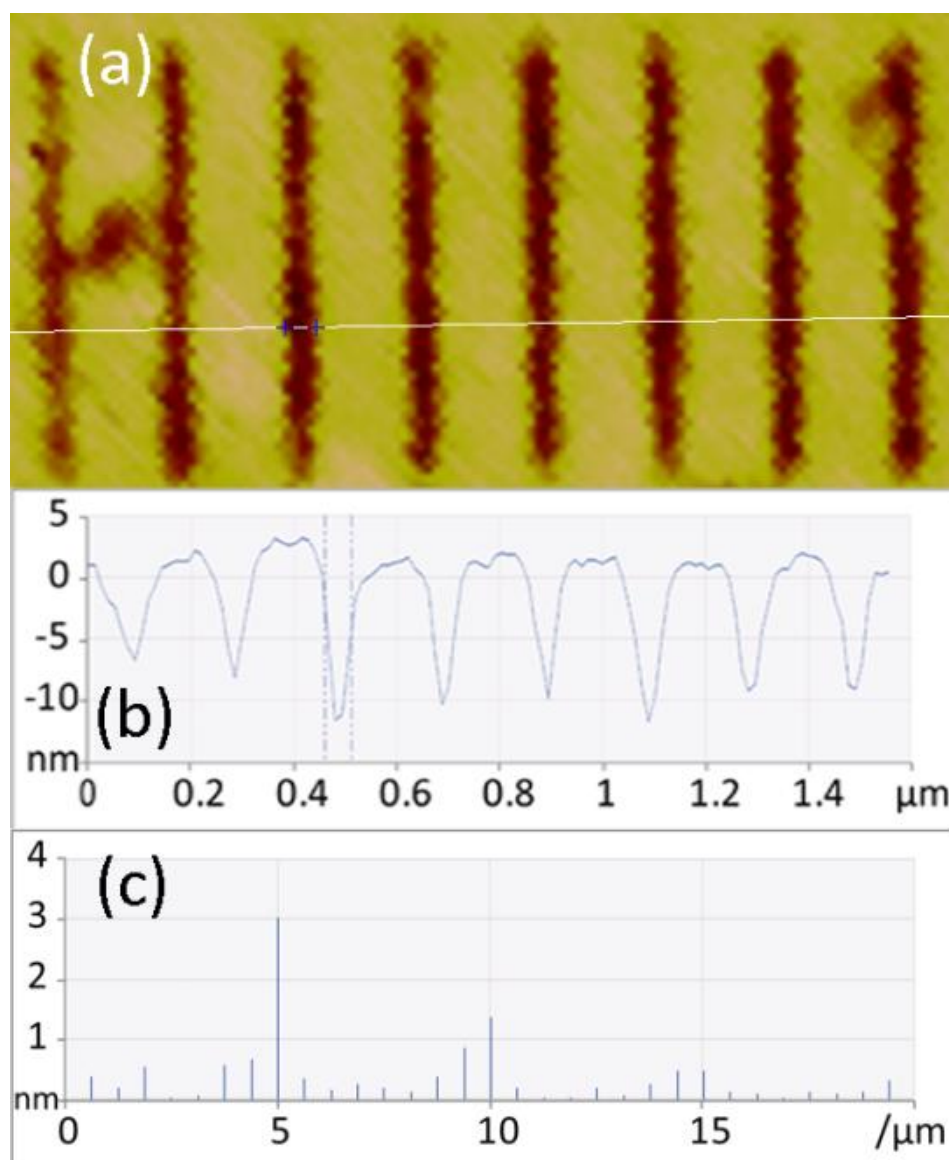
Fig. 5-5. AFM image of developed pattern on control sample (a) AFM image of 200 nm period grating; (b) cross section curve shows the image depth of 10nm; (c) Fourier analysis shows a peak at 5 μm^{-1}, corresponding to 200 nm pitch.

5.4 Simulation and discussion

To verify the performance of our Al superlens sample working at 193nm DUV wavelength, we performed the Finite-difference time-domain (FDTD) simulation using Lumerical software. Figure 5-6 shows the simulation configuration, in XY plane view. The FDTD simulation region and different material for each layer are indicated. The boundary conditions are set to be "Period" in X direction, and "perfect matching layer (PML)" in Y direction, so drawing 2 periods of tungsten (W) grating is adequate for the simulation. As the dimension of W grating in Z direction is much larger than the dimensions in X and Y directions, 2-D simulation in the XY plane will be accurate. The mesh accuracy is set to be 0.5nm in both X and Y directions. A plane wave light source in the TM polarization is launched from the quartz substrate, with the amplitude of E field set to be unity and the wavelength set to be 193nm.

After simulation, each component of the Poynting vector of the light beam coming out of the Al superlens layer is plotted, so that we can evaluate the superlens performance and explore the underpinning physics. We compared the performances by changing the thickness of different layers and changing the period of the W grating, to find the optimized parameters and the limitation of the superlens. The performances of the controlled samples are also simulated. The details will be discussed in following paragraphs.

First, we analyzed the superlens performance with 20nm W, 13nm Al and 15nm SiO_2. The pattern on the W mask layer is 50nm half-pitch (100nm period) grating, which is one of the standard patterns to characterize the performance of a lithography technology. Figure 5-7 shows the 2D intensity plots of three important components of the Poynting vectors in the simulation region.
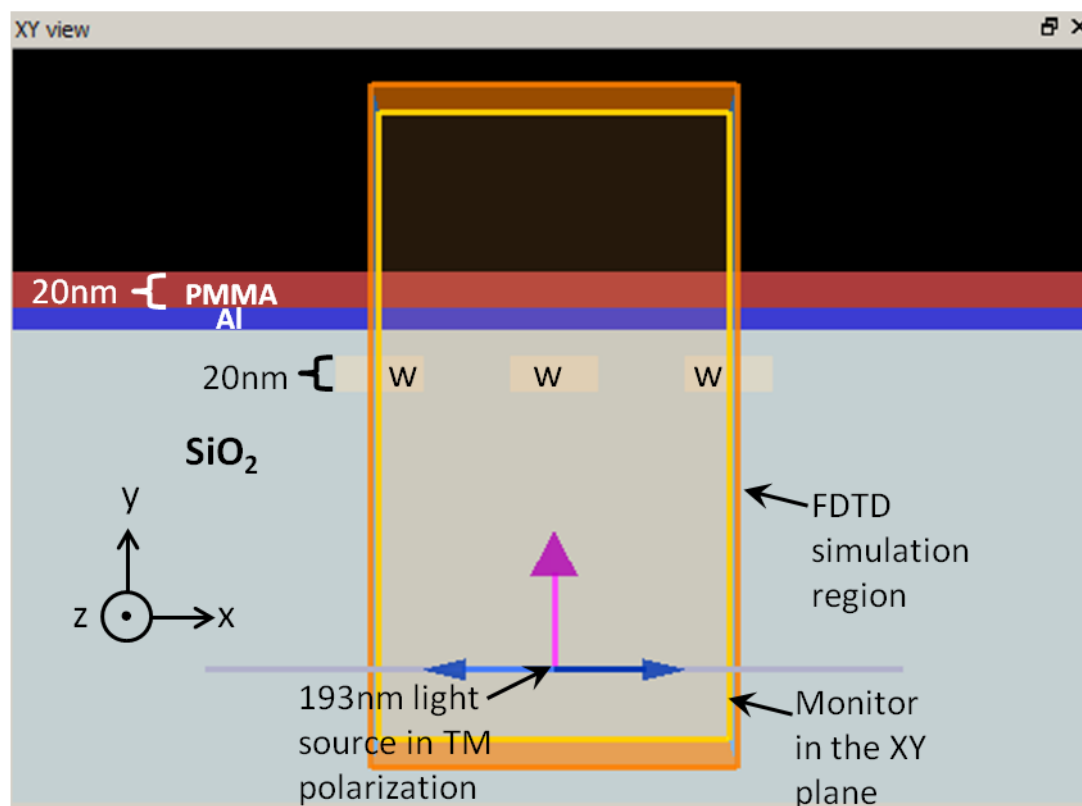
Fig. 5-6. Environmental settings of the FDTD simulation in Lumerical software.
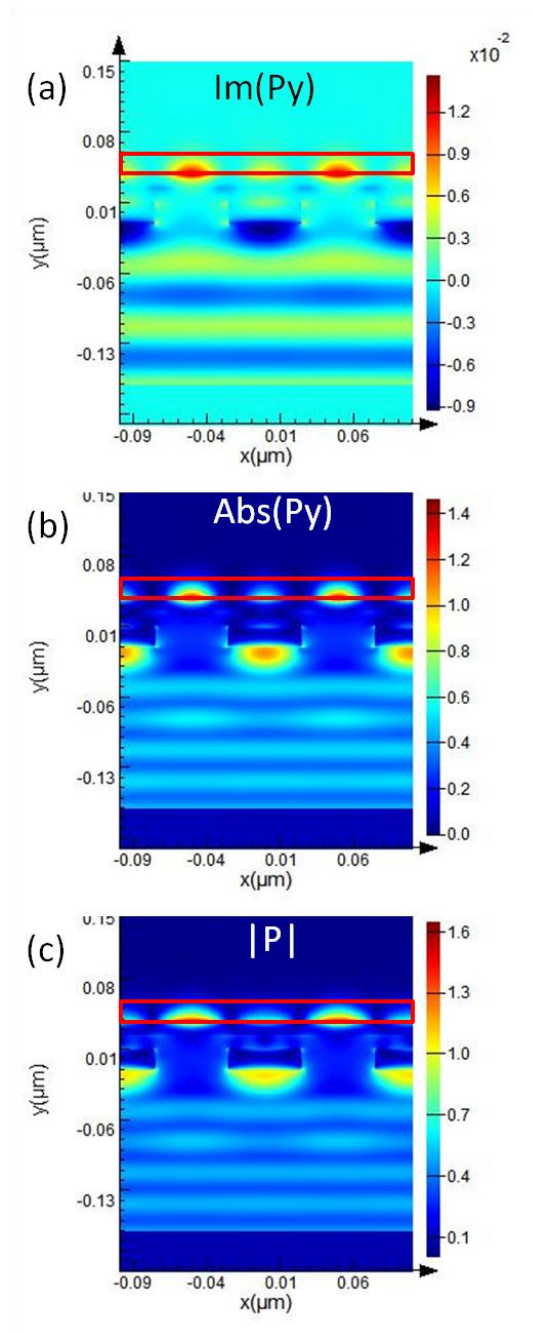
Fig. 5-7. 2D intensity plots of three important components of the Poynting vectors in the simulation region. (a) imaginary part of the Py component; (b) absolute value of the Py component; (c) the magnitude of the Poynting vector. (red squares indicate the locations of PMMA resist)

Fig. 5-8. Simulated performance of the Superlens sample with 20nm thick 50nm HP W grating, 13nm Al, 15nm SiO_2 and 20nm PMMA. Three components of the Poynting vectors at different distances into the PMMA: (a) imaginary part of the *Py* component; (b) absolute value of the *Py* component; (c) the magnitude of the Poynting vector; (d) diagram of the W mask layer indicating the openings and blocks.

Lumerical defines the imaginary part of a Poynting vector the evanescent wave in near field, and the real part the traveling wave. [125]

Figure 5-8 (a),(b),(c) represent the imaginary component of the *Py* (Poynting vector in the Y direction), the absolute value of the *Py*, and the magnitude of the whole Poynting vector |*P*|, respectively, at different distance into the PMMA (red square region in Fig. 5-7). Figure 5-8 (d) indicates the relative position of the W grating in the mask layer. Plotting these values in curves will ease the comparison of the intensity. Figure 5-8 (a),(b) are almost identical in both height and curve shape, indicating the real component of the *Py* is negligible. Comparing Fig. 5-8(b) and (c), we find the heights of the curves are close, leaving the only difference in the broadened shape of the peaks in the |*P*| plot, which proves that the *Px* component does not contribute to the light intensity, but only widens the light beam profile, which we want to avoid for high resolution imaging. From the above comparisons, we can tell that the evanescent wave in the light propagation direction Im(*Py*) constitutes the main part of the light beam after transmitting through the superlens, which agrees with the discussion in the introduction section and the references [117-120, 126]. The *Px* component does not contribute to the superlens performance, but broadening the linewidth. In the curves of Fig. 5-8, we also see the side-lobes on top of the W mask region. We believe they are caused by the exited standing evanescent wave modules, forming the well-known surface Plasmon (SP) near the metal surface. The side-lobes of the adjacent main peaks overlap with each, forming the obvious secondary peaks on top of the W mask region. As the side peaks are about half of the primary peaks, by controlling the development temperature after the DUV exposure, we can still get high contrast images.
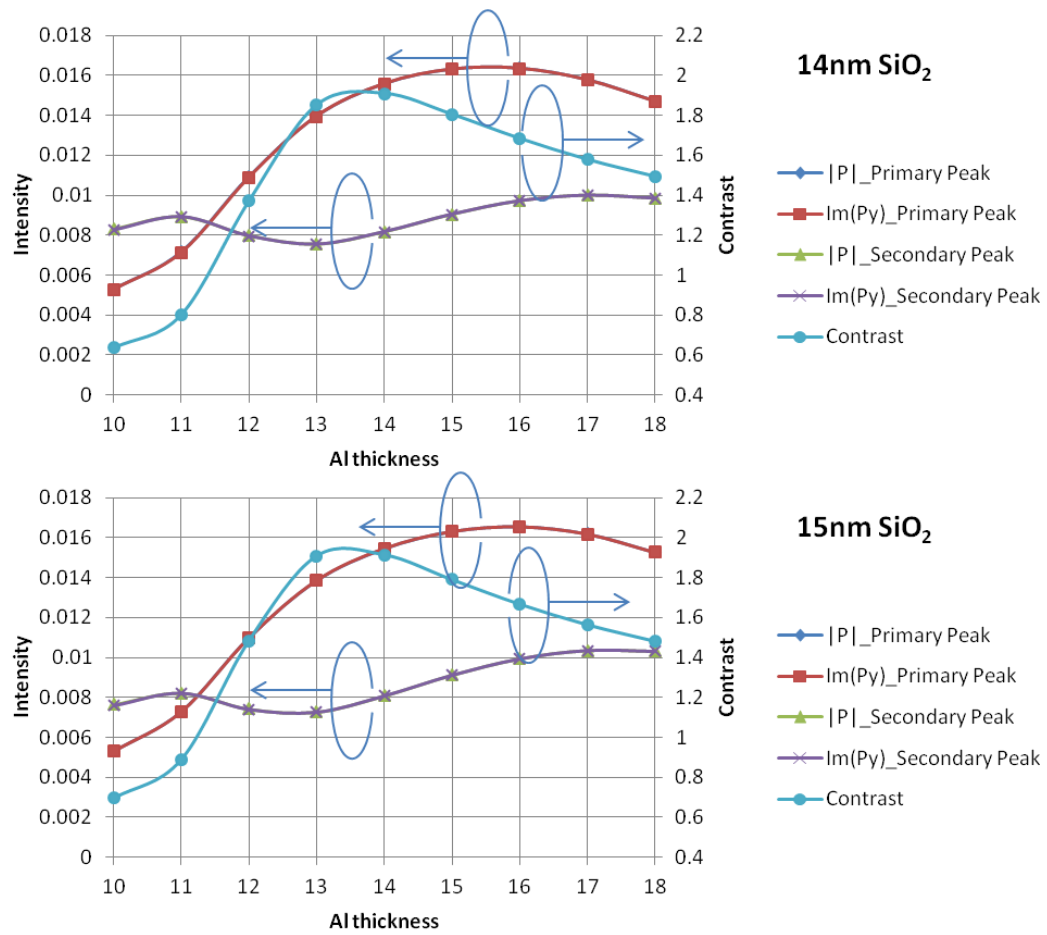
Fig. 5-9. Variation of the primary peak value, secondary peak value and their contrast of Im(**Py**) and |**P**| with the change of Al thickness, while the SiO$_2$ thickness is fixed to be 14nm and 15nm.

After studying the physics of the superlens, we want to find the optimized thicknesses of the Al layer and SiO_2 layer.

We performed similar simulations by changing one single parameter, the Al thickness, from 13nm to 18nm. The simulations show similar plots of curves as Fig. 5-8, with slightly difference in the heights of the peaks. In Fig. 5-8, we plot the changing trends of the primary peak value and secondary peak value of Im(Py) and $|P|$ curves with the variation of Al thickness. $|P|$ and Im(Py) curves, both the primary and secondary peaks, overlap perfectly with each other, agreed well with the conclusion of Fig. 5-8. The plots show that the Al thickness of 16nm produces the highest Poynting vector intensity. As we know, metal enhances the evanescent wave [126], and also absorbs the EM wave when the light penetrates through it. The 16nm Al balances between the enhancement and the absorption, producing the highest peak intensity. We also plot the contrast between the primary and secondary peak. Simulation shows 14nm Al will produce best image contrast.

Then, another series of simulations were performed to analyze how the thickness of the SiO_2 layer will change the performance of the superlens. Figure 5-10 plots the variation of the primary and secondary peak values of Im(Py) and $|P|$ with the change of SiO_2 thickness, as well as the contrast between the primary and secondary peaks, while the Al thickness is fixed to be 14 nm. The result shows 15nm SiO_2 produces optimized contrast.

So far, we proved that our experimental results agree with the simulation, for the 50nm HP grating pattern. It would be of interest to further analyze the performance of the superlens for smaller features, which were not successfully produced in our exposure.
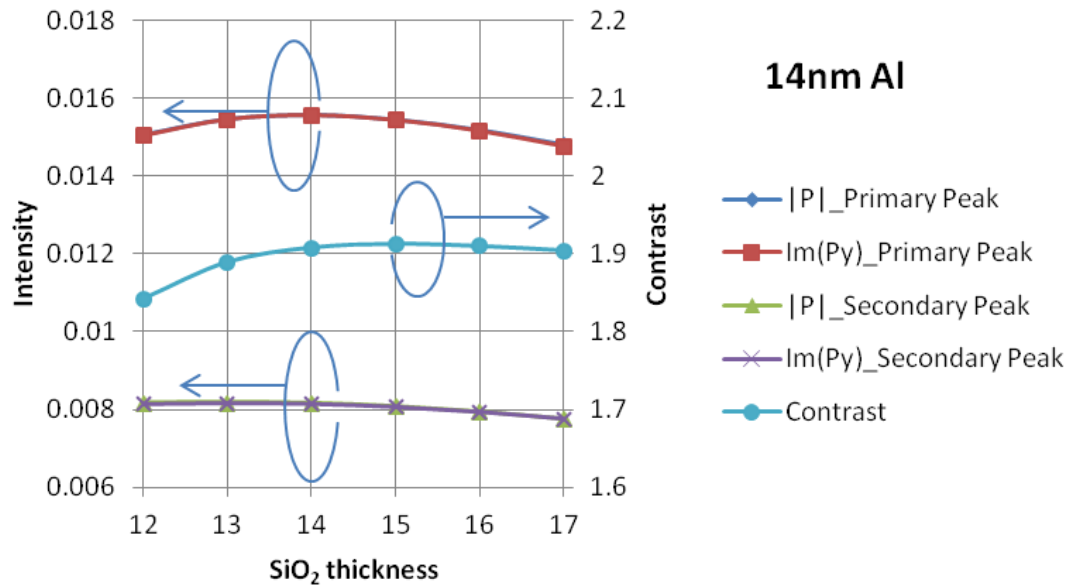
Fig. 5-10. Variation of the primary peak value, secondary peak value and their contrast of Im(*Py*) and |*P*| with the change of SiO$_2$ thickness, while the Al thickness is fixed to be 14nm.
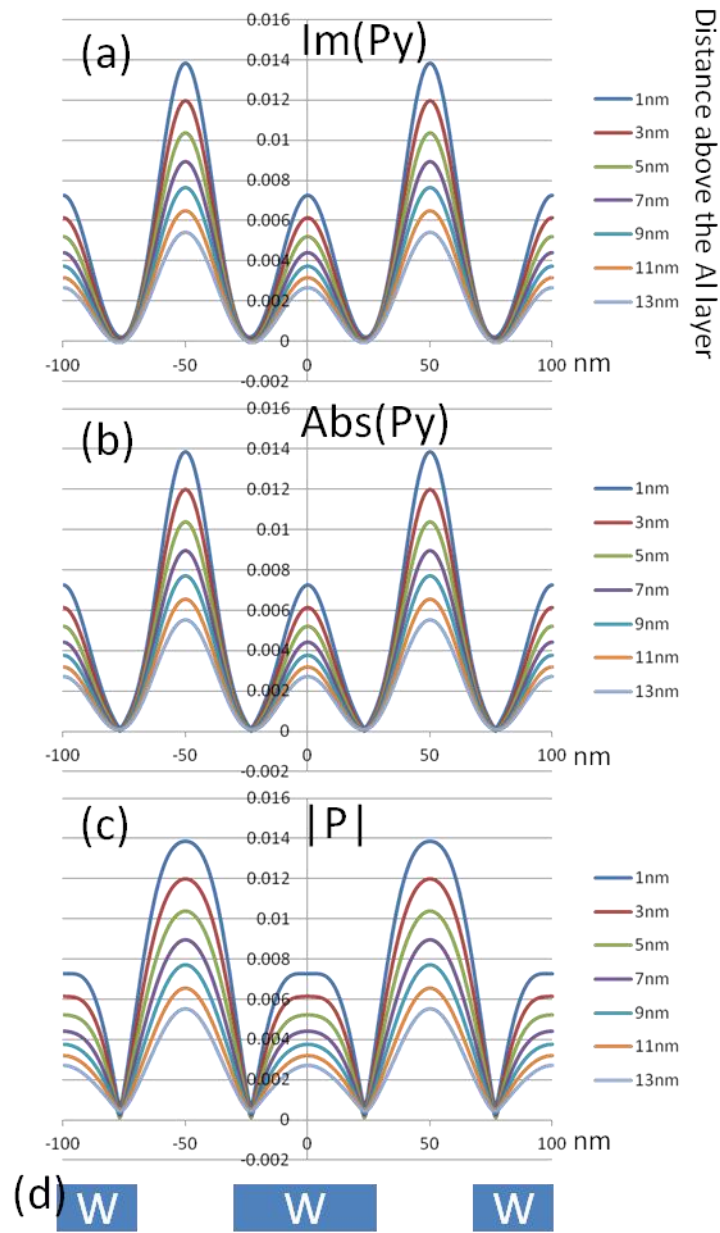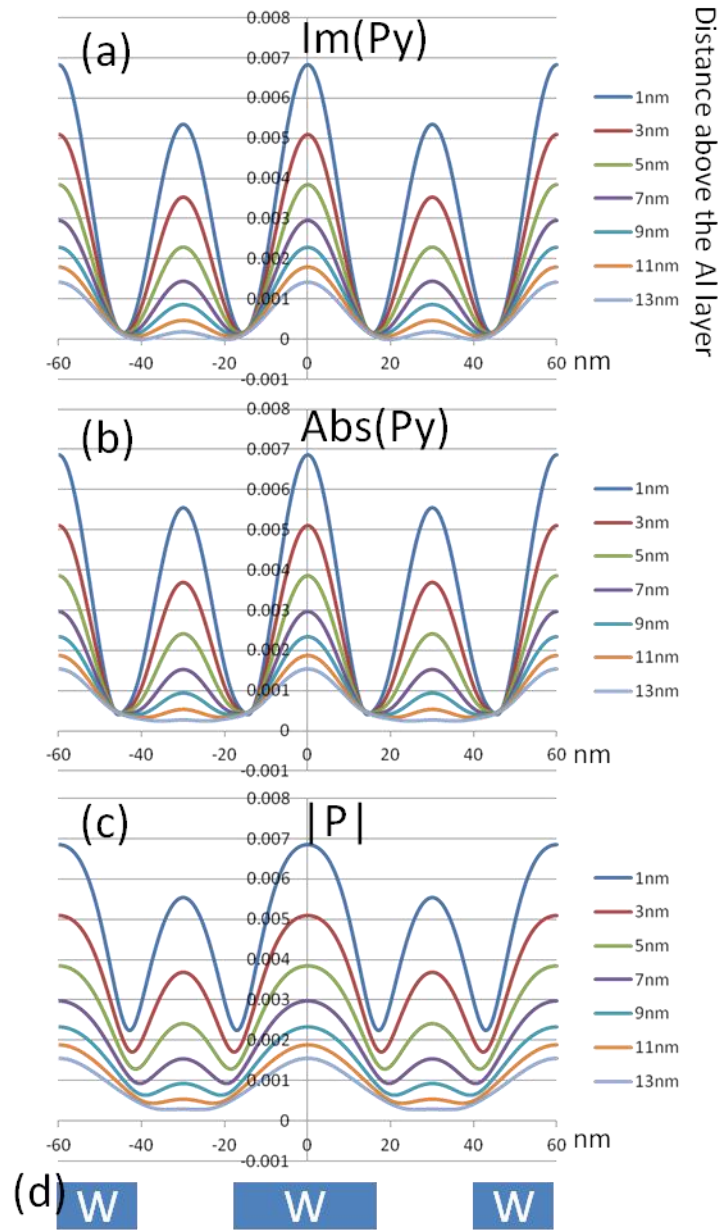
Fig. 5-11. Simulated performance of the Superlens sample with 20nm thick 30nm HP W grating, 13nm Al, 15nm SiO_2 and 20nm PMMA. Three components of the Poynting vectors at different distances above the sample: (a) imaginary part of the Py; (b) absolute value of the Py; (c) the magnitude of the Poynting vector $|P|$; (d) diagram of the W mask layer indicating the openings and blocks.

We did further simulation by keeping the 20nm, 13nm and 15nm W, Al and SiO_2 thicknesses respectively, while changing the W grating HP to 30nm.

The simulation results are plotted in Fig. 5-11. Figure 5-11 (a),(b),(c) represent the imaginary component of the *Py*, the absolute value of the *Py*, and the magnitude of the whole Poynting vector |*P*|, respectively. Figure 5-11 (d) indicates the relative position of the 30nm HP W grating in the mask layer. The first phenomena we observe is the primary peaks are above the W blocks, instead of the W openings. Secondly, the intensity of the peaks is less than half of the 50nm HP case. What makes the situation worse is the secondary peaks are as strong as the primary peaks, and the valleys are not weak enough to yield enough contrast. Over all, we will get a relatively uniformed exposure in this simulation condition, which agrees the experimental results, only a plane exposed pattern was observed.

We also want to confirm the performance of the control samples, which have the Al layer replaced by SiO_2. The simulation parameters are 20nm W grating with 100nm HP, 28nm SiO_2 and 20nm PMMA. Figure 5-12 plots the simulation results, the real part of the *Py* [Fig. 5-12(a)]; imaginary part of the *Py* [Fig. 5-12(b)]; absolute value of the *Py* [Fig. 5-12(c)]; and the magnitude of the Poynting vector |*P*| [Fig. 5-12(d)]. The result shows the real part of *Py* contributes significantly to the *Py*, which also determines the shape of the |*P*|. This result well describes the mechanism of traditional lithography. The fact that 100nm feature size equals the half of the wavelength (193nm) shows the diffraction limitation of the traditional lithography technology. And feature size beyond 100nm, like 50nm HP grating, is not achievable using this technology. The result is shown in Fig. 5-13, showing a flat and weak |*P*| profile. The reason is the intensity of Re(*Py*) and Im(*Py*)
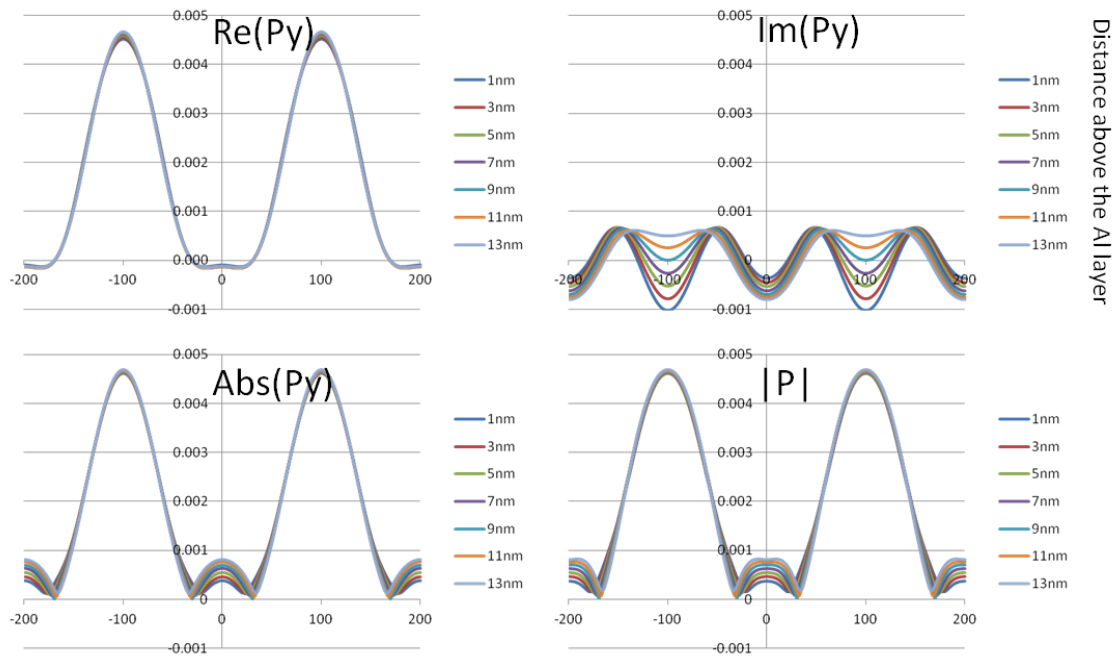
Fig. 5-12. Simulated performance of the control sample with 20nm thick 100nm HP W grating, 28nm SiO_2 and 20nm PMMA. Four components of the Poynting vectors at different distances above the sample: (a) real part of the Py; (b) imaginary part of the Py; (c) absolute value of the Py; (d) the magnitude of the Poynting vector $|P|$.
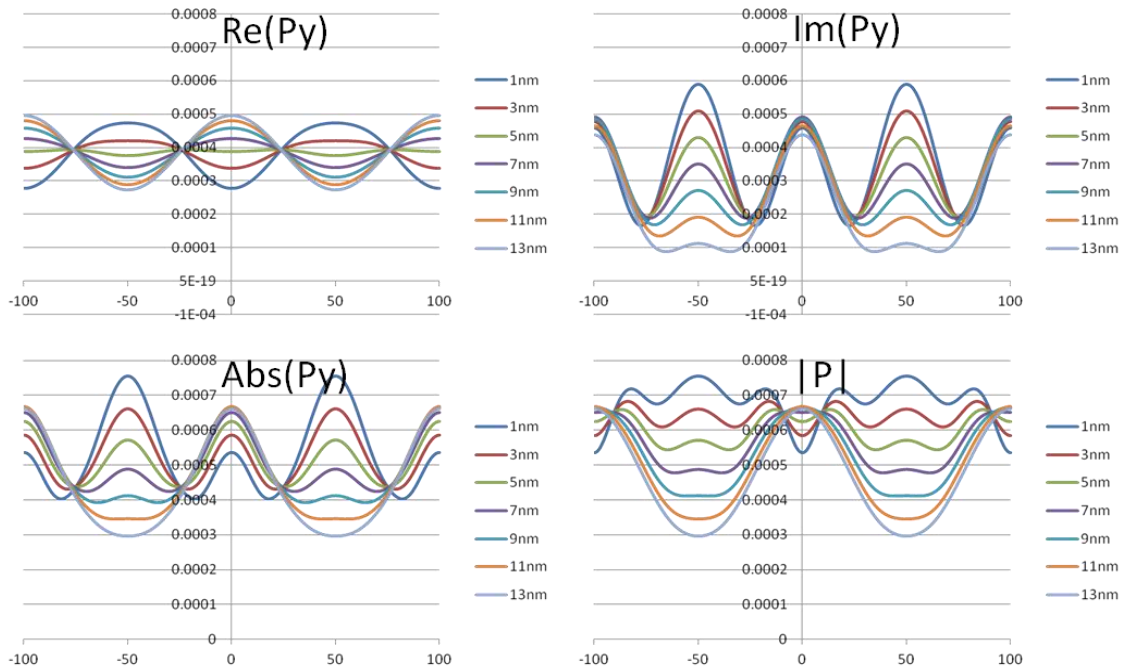
Fig. 5-13. Simulated performance of the control sample with 20nm thick 50nm HP W grating, 28nm SiO$_2$ and 20nm PMMA. Four components of the Poynting vectors at different distances above the sample: (a) real part of the *Py*; (b) imaginary part of the *Py*; (c) absolute value of the *Py*; (d) the magnitude of the Poynting vector |*P*|.

are equally low, along with the low contrast.

5.5 Conclusions

Different from previously widely reported silver superlens, we demonstrated an Al superlens working at 193 nm DUV. 50nm half pitch grating, 50 nm spacing 50 nm width double slits images are achieved by exposing PMMA resist. By carefully comparing the experimental and simulation results, we evaluated the superlens performance and investigated the underpinning physics, and presented some trends showing how the Al and SiO_2 thickness can affect the image quality. Also, operation temperature of the development after DUV exposure is critical to achieve the high contrast images. We want to emphasize that our 193 nm DUV exposure setup is low cost, non-toxic and compact, which is favored by lab experiments.

Chapter 6. Conclusions and suggestions for future work

6.1 Conclusions

Si photonics has a bright future in the applications of telecommunication, interconnects and sensors, because of its potential of low cost high volume manufacturing capability and ease to integrate with CMOS electronic circuits. Significant progress was made and some promising products were launched. In the meanwhile, the demand for more power efficient, more compact products is endless. So researchers are continuously inventing novel devices, among which, the PCW is one of the most attractive devices. The research of all its properties is contributive.

In this dissertation, we have experimentally demonstrated the control of excitation symmetry for an odd TE-like mode in a PCW. An odd-mode Mach-Zehnder coupler is utilized to selectively excite the odd mode with a contrast >20 dB over the background. Assisted by a mixed-mode MZC, slow-light mode beating is observed and is utilized to measure the group index of this odd mode.

Also, the evolution of the PCW transmission spectrum in the odd mode band is studied under electro-optic tuning. The shift of the odd-mode band under carrier injection has been observed through interband scattering. The band shift is determined statistically from the measured spectrum with noise. The spectral shift was accounted for by electro-optic and thermo-optic effects. The impact of interband scattering for the PCW based isolator application is analyzed and potential remedies are discussed.

To make reliable nano-devices by the method of semiconductor fabrication, the lithography process is one of the most critical technologies. NIM and the related superlens structure are a good candidate of the next generation of lithography technology

for the 22nm node, as it enhances the near field evanescent wave and is able to overcome the half wavelength diffraction limitation. Different from previously widely reported silver superlens, we demonstrated an Al superlens working at 193nm DUV. 50nm half pitch grating, 50nm spacing 50nm width double slits and 67nm line width "RU" letter images were achieved by exposing PMMA resist. By carefully comparing the experimental and simulation results, we analyzed the superlens performance and investigated the underpinning physics, and presented some trends showing how the Al and SiO_2 thickness can affect the image quality. Also, operation temperature of the development after DUV exposure is critical to achieve the high contrast images. We want to emphasize that our 193nm DUV exposure setup is low cost, non-toxic and compact, which is favored by lab experiments.

6.2 Suggestions for future work

For research that intends to utilize the TE odd mode in the PCW photonics band, MZC is an efficient way to generate the TE odd mode with high purity, while keeping the propagation loss low. Design of the length difference between the two arms should be based on the calculation for different working wavelength.

In the research of PCW based optical isolator, the interband scattering should be avoided, which requires more fabrication accuracy to produce more uniform air hole array with smoother side wall for the air holes. Fortunately, CFN provides high end nano-fabrication tools. Especially, the new developed HBr based ICP etching process, using HSQ as the E-beam lithography resist and etching resistance layer, produces more advanced side wall conditions.

Following the superlens design provided by an external group, our devices produced fine 50nm feature size, but it is lower than our best expectation, 20nm feature size. Follow-up simulations by ourselves confirmed the performance of devices and showed that even 30nm feature size is not achievable based on current design. For future research, a systematic simulation should be done prior the fabrication, to find the optimized parameter to achieve smaller feature sizes. To improve fabrication precision, a more reliable characterization method should be applied to precisely measure the thickness of each layer in the device. Meanwhile, detailed comparison experiments should be carried out to find the best development temperature after the DUV exposure. There should be a best combination of developing time and temperature to produce the best image contrast. Before the superlens lithography technology can be used in real applications, random patterns with small feature size should be imaged precisely. Based on our experiments, I believe the Proximity Effect Correction (PEC) process has to be done on the designed pattern, to remove the rounded corners and non-uniform line-width.

References

[1] R. A. Soref, and J. Lorenzo, "All-silicon active and passive guided-wave components for λ = 1.3 and 1.6 μm," IEEE J. Quantum Electron., Vol. QE-22, No. 6, pp. 873–879, Jun. 1986;

[2] R. A. Soref, and B. R. Bennett, "Kramers–Kronig analysis of E–O switching in silicon," SPIE Integr. Opt. Circuit Eng., 1986, Vol. 704, pp. 32–37;

[3] B. Schuppert, J. Schmidtchen, and K. Petermann, "Optical channel waveguides in silicon diffused from GeSi alloy," Electron. Lett., Vol. 25, No. 22, pp. 1500–1502, Oct. 1989;

[4] R. A. Soref, J. Schmidtchen, and K. Petermann, "Large single-mode rib waveguides in GeSi and Si-on-SiO$_2$," IEEE J. Quantum Electron, Vol. 27, No. 8, pp. 1971–1974, Aug. 1991;

[5] P. D. Trinh, S. Yegnanarayanan, and B. Jalali, "Integrated optical directional couplers in silicon-on-insulator," Electron. Lett., Vol. 31, No. 24, pp. 2097–2098, Nov. 1995;

[6] U. Fischer, T. Zinke, and K. Petermann, "Integrated optical waveguide switches in SOI," IEEE Int. SOI Conf., pp. 141–142, Oct. 1995;

[7] T. T. H. Eng, S. S. Y. Sin, S. C. Kan, and G. K. L. Wong, "Surface micromachined movable SOI optical waveguides," Int. Conf. Solid-State Sens. Actuators, Vol. 1, pp. 348–350, 1995;

[8] C. Z. Zhao, G. Z. Li, E. K. Liu, Y. Gao, and X. D. Liu, "Silicon on insulator Mach–Zehnder waveguide interferometers operating at 1.3 μm," Appl. Phys. Lett., Vol. 67, No. 17, pp. 2448–2449, Oct. 1995;

[9] P. D. Trinh, S. Yegnanarayanan, and B. Jalali, "5 $\times$ 9 integrated optical star coupler in silicon-on-insulator technology," IEEE Photon. Technol. Lett., Vol. 8, No. 6, pp. 794–796, Jun. 1996;

[10] P. D. Trinh, S. Yegnanarayanan, F. Coppinger, and B. Jalali, "Silicon on-insulator (SOI) phased-array wavelength multi-demultiplexer with extremely low-polarization sensitivity," IEEE Photon. Technol. Lett., Vol. 9, No. 7, pp. 940–942, Jul. 1997;

[11] B. Jalali, S. Yegnanarayanan, T. Yoon, T. Yoshimoto, I. Rendina, and F. Coppinger, "Advances in silicon-on-insulator optoelectronics," IEEE J. Sel. Topics Quantum Electron., Vol. 4, No. 6, pp. 938–947, Nov./Dec. 1998;

[12] B. Jalali, "Silicon Photonics," J. Lightwave Tech., Vol. 24, No. 12, Dec. 2006;

[13] B. Jalali, M. Paniccia, and G. Reed, "Silicon Photonics," IEEE microwave magazine, Vol. 6, pp. 1527-3342, Jun. 2006;

[14] E. Mohammed, A. Alduino, T. Thomas, H. Braunisch, D. Lu, J. Heck, A. Liu, I. Young, B. Barnett, G. Vandentop, and R. Mooney, "Optical interconnect system integration for ultra short reach applications," Intel. Technol. J., Vol. 8, pp. 115–127, 2004;

[15] N.M. Jokerst, M.A. Brooke, S. Cho, M. Thomas, J. Lillie, D. Kim, S. Ralph, and K. Dennis, "Integrated planar lightwave bio/chem OEIC sensors on Si CMOS circuits," Proc. SPIE, Vol. 5730, pp. 226–233, 2005;

[16] Y. A. Vlasov, "Silicon Integrated Nanophotonics: Road from Scientific Explorations to Practical Applications," Plenary Presentation at CLEO/QELS Conference, 2012;

[17] D. Liang, and J. E. Bowers, "Recent progress in lasers on silicon," Nature Photon., Vol. 4, pp. 511-517, Aug. 2010;

[18] H. Rong, et al., "Low-threshold continuous-wave Raman silicon laser," Nature Photon., Vol. 1, pp. 232–237, 2007;

[19] J. Liu, X. Sun, R. Camacho-Aguilera, L. C. Kimerling, and J. Michel, "Ge-on-Si laser operating at room temperature," Opt. Lett. Vol. 35, pp. 679–681, 2010;

[20] R. E. Camacho-Aguilera, Y. Cai, N. Patel, J. T. Bessette, M. Romagnoli, L. C. Kimerling, and J. Michel, "An electrically pumped germanium laser," Optics Express, Vol. 20, No. 10, May 2012;

[21] Yole Developpement's online article, "Huge Market Potential for Silicon Photonics?";

[22] R. Won, M. Paniccia, "Integrating silicon photonics," Nature Photon., Vol. 4, pp 498-499, Aug. 2010;

[23] Fengnian Xia, Lidija Sekaric, and Yurii Vlasov, "Ultracompact optical buffers on a silicon chip," Nat. Photon., Vol. 1, pp. 65, Jan. 2007;

[24] Folkert Horst, William M. J. Green, Bert Jan Offrein, and Yurii A. Vlasov, "Silicon-on-Insulator Echelle Grating WDM Demultiplexers With Two Stigmatic Points," IEEE Photon. Tech. Lett., Vol. 21, No. 23, pp. 1743, Dec. 2009;

[25] Solomon Assefa, William M. J. Green, Alexander Rylyakov, Clint Schow, Folkert Horst and Yurii A. Vlasov, "CMOS Integrated Nanophotonics-Enabling Technology for Exascale Computing Systems," OFC invited talk, OMM6, 2011;

[26] J. C. Rosenberg, W. M. J. Green, S. Assefa, T. Barwicz, M. Yang, S. M. Shank, and Y. A. Vlasov, "Low-Power 30 Gbps Silicon Microring Modulator," CLEO PDPB9, 2011;

[27] Ansheng Liu, Ling Liao, Doron Rubin, Hat Nguyen, Berkehan Ciftcioglu, Yoel Chetrit, Nahum Izhaky, and Mario Paniccia, "High-speed optical modulation based on carrier depletion in a silicon waveguide," Opt. Exp., Vol. 15, No. 2, pp. 660, Jan. 2007;

[28] Delphine Marris-Morini, Laurent Vivien, Jean Marc Fédéli, Eric Cassan, Philippe Lyan, and Suzanne Laval, "Low loss and high speed silicon optical modulator based on a lateral carrier depletion structure," Opt. Exp., Vol. 16, No. 1, pp. 334, Jan. 2008;

[29] S. J. Spector, M. W. Geis, G.-R.Zhou, M. E. Grein, F. Gan, M.A. Popović, J. U. Yoon, D. M. Lennon, E. P. Ippen, F. X. Kärtner, and T. M. Lyszczarz, "CMOS-compatible dual-output silicon modulator for analog signal processing," Opt. Exp., Vol. 16, No. 15, pp. 11027, Jul. 2008;

[30] Jeong Woo Park, Jong-Bum You, In Gyoo Kim, and Gyungock Kim, "High-modulation efficiency silicon Mach-Zehnder optical modulator based on carrier depletion in a PN Diode," Opt. Exp., Vol. 17, No. 18, pp. 15520, Aug. 2009;

[31] Po Dong, Shirong Liao, Dazeng Feng, Hong Liang, Dawei Zheng, Roshanak Shafiiha, Cheng-Chih Kung, Wei Qian, Guoliang Li, Xuezhe Zheng, Ashok V. Krishnamoorthy, and Mehdi Asghari, "Low Vpp, ultralow-energy, compact, high-speed silicon electro-optic modulator," Opt. Exp., Vol. 17, No. 25, Dec. 2009;

[32] Tsung-Yang Liow, Kah-Wee Ang, Qing Fang, Jun-Feng Song, Yong-Zhong Xiong, Ming-Bin Yu, Guo-Qiang Lo, and Dim-Lee Kwong, "Silicon Modulators and Germanium Photodetectors on SOI: Monolithic Integration, Compatibility, and Performance Optimization," JST Quantum Electron., Vol. 16, No. 1, pp. 307, Jan. 2010;

[33] Douglas M. Gill, Sanjay S. Patel, Mahmoud Rasras, Kun-Yii Tu, Alice E. White, Young-Kai Chen, Andrew Pomerene, Daniel Carothers, Robert L. Kamocsai, Craig M. Hill, and James Beattie, "CMOS-Compatible Si-Ring-Assisted Mach–Zehnder Interferometer With Internal Bandwidth Equalization," JST Quantum Electron., Vol. 16, No. 1, pp. 45, Jan. 2010;

[34] Michael R. Watts, William A. Zortman, Douglas C. Trotter, Ralph W. Young, and Anthony L. Lentine, "Low-Voltage, Compact, Depletion-Mode, Silicon Mach–Zehnder Modulator," JST Quantum Electron., Vol. 16, No. 1, pp. 159, Jan. 2010;

[35] Junichi Fujikata, Jun Ushida, Yu Ming-Bin, Zhu ShiYang, Ding Liang, Patrick Lo Guo-Qiang, Dim-Lee Kwong, and Takahiro Nakamura, "25 GHz Operation of Silicon Optical Modulator with Projection MOS Structure," OFC OMI3, 2010;

[36] B. Guha, K. Preston, and M. Lipson, "Athermal silicon microring electro-optic modulator," Opt. Lett., Vol. 37, No. 12, pp. 2253, Jun. 2012;

[37] A. Nitkowski, A. Baeumner, and M. Lipson, "On-chip spectrophotometry for bioanalysis using microring resonators," Biomed. Opt. Express, Vol. 2, No. 2, 01 Feb. 2011;

[38] S. G. Johnson, "Photonic Crystals: From Theory to Practice," Ph.D. thesis, 2001.

[39] Y. Shani, C. H. Henry, R. C. Kistler, K. J. Orlowsky, and D. A. Ackerman, "Efficient coupling of a semiconductor laser to an optical fiber by means of a tapered waveguide on silicon," App. Phys. Lett., Vol. 55, 2389, 1989;

[40] T. Shoji, T. Tsuchizawa, T. Watanabe, K. Yamada, and H. Morita, "Low loss mode size converter from 0.3 μm square Si wire waveguides to single mode fibers," Electron. Lett., Vol. 38, 1669, 2002;

[41] V. Almeida, R. Panepucci, and M. Lipson, "Nanotaper for compact mode conversion," Opt. Lett., Vol. 28, 1302, 2002;

[42] Sharee McNab, Nikolaj Moll, and Yurii Vlasov, "Ultra-low loss photonic integrated circuit with membrane-type photonic crystal waveguides," Opt. Exp., Vol. 11, No. 22, pp. 2927-2939, Nov. 2003;

[43] Babak Momeni, Ali Asghar Eftekhar, and Ali Adibi, "Effective impedance model for analysis of reflection at the interface of photonic crystals," Opt. Lett., Vol. 32, No. 7, Apr. 2007;

[44] Amir Hosseini, Xiaochuan Xu, David N. Kwong, Harish Subbaraman, Wei Jiang, and Ray T. Chen, "On the role of evanescent modes and group index tapering in slow light photonic crystal waveguide coupling efficiency," Appl. Phys. Lett., Vol. 98, 031107, 2011;

[45] Che-Yun Lin, Xiaolong Wang, Swapnajit Chakravarty, Beom Suk Lee, Wei-Cheng Lai, and Ray T. Chen, "Wideband group velocity independent coupling into slow light silicon photonic crystal waveguide," Appl. Phys. Lett., Vol. 97, 183302, 2010;

[46] Xiaonan Chen, Wei Jiang, Jiaqi Chen, Lanlan Gu, and Ray T. Chen, "20 dB-enhanced coupling to slot photonic crystal waveguide using multimode interference coupler," Appl. Phys. Lett., Vol. 91, 091111, 2007;

[47] Steven G. Johnson, Pierre R. Villeneuve, Shanhui Fan, and J. D. Joannopoulos, "Linear waveguides in photonic-crystal slabs," Phys. Rev. B, Vol. 62, No. 12, 8212, Sep. 2000;

[48] Yurii A. Vlasov, and Sharee J. McNab, "Coupling into the slow light mode in slab-type photonic crystal waveguides," Opt. Lett., Vol. 31, No. 1, pp. 50-52, Jan. 2006;

[49] E. Kuramochi, M. Notomi, S. Hughes, A. Shinya, T. Watanabe, and L. Ramunno, "Disorder-induced scattering loss of line-defect waveguides in photonic crystal slabs," Phys. Rev. B, Vol. 72, No. 16, 161318, 2005;

[50] Weiwei Song, Ryan A. Integlia, and Wei Jiang, "Slow light loss due to roughness in photonic crystal waveguides: An analytic approach," Phys. Rev. B, Vol. 82, 235306, 2010;

[51] Yu. A. Vlasov, N. Moll, and S. J. McNab, "Mode mixing in asymmetric double-trench photonic crystal waveguides," J. Appl. Phys. Vol. 95, No. 9, May 2004;

[52] X. Chen, Y. S. Chen, Y. Zhao, W. Jiang, and R. T. Chen, "0.54 pJ/bit Capacitor-Embedded Silicon Slot Photonic Crystal Waveguide Modulator," Opt. Lett., Vol. 34, 602-604, 2009;

[53] Solomon Assefa, Sharee J. McNab, and Yurii A. Vlasov, "Transmission of slow light through photonic crystal waveguide bends," Opt. Lett, Vol. 31, No. 6, pp.745-747, Mar. 2006;

[54] Masaya Notomi, Akihiko Shinya, Koji Yamada, Jun-ichi Takahashi, Chiharu Takahashi, and Itaru Yokohama, "Structural tuning of guiding modes of line-defect waveguides of Silicon-on-Insulator photonic crystal slabs," IEEE J. Quan. Electron., Vol. 38, No. 7, Jul. 2002;

[55] Norihiro Ishikura, Ryo Hosoi, Ryo Hayakawa, Takemasa Tamanuki, Mizuki Shinkawa, and Toshihiko Baba, "Photonic crystal tunable slow light device integrated with multi-heaters," Appl. Phys. Lett., Vol. 100, 221110, 2012;

[56] M. Notomi, K. Yamada, A. Shinya, J. Takahashi, C. Takahashi, and I. Yokohama, "Extremely large group-velocity dispersion of line-defect waveguides in photonic crystal slabs," Phys. Rev. Lett., Vol. 87, No. 25, 253902, Dec. 2001;

[57] Eric Dulkeith, Sharee J. McNab, and Yurii A. Vlasov, "Mapping the optical properties of slab-type two-dimensional photonic crystal waveguides," Phys. Rev. B, Vol. 72, No. 11, 115102, 2005;

[58] Toshihiko Baba, "Slow light in photonic crystals," Nature Photonics, Vol. 2, pp. 465-473, Aug. 2008;

[59] L. Gu, W. Jiang, X. Chen, L. Wang, and R. T. Chen, "High-speed silicon photonic crystal waveguide modulator for low-voltage operation," Appl. Phys. Lett., Vol. 90, 071105, 2007;

[60] Hong C. Nguyen, Satoshi Hashimoto, Mizuki Shinkawa and Toshihiko Baba, "Compact and fast photonic crystal silicon optical modulators," Opt. Exp., Vol. 20, No. 20, Sep. 2012;

[61] Xuetao Gan, Ren-Jye Shiue, Yuanda Gao, Kin Fai Mak, Xinwen Yao, Luozhou Li, Attila Szep, Dennis Walker, Jr., James Hone, Tony F. Heinz, and Dirk Englund,

"High-Contrast Electrooptic Modulation of a Photonic Crystal Nanocavity by Electrical Gating of Graphene," Nano Lett., Vol. 13, 691-696, 2013;

[62] Arka Majumdar, Jonghwan Kim, Jelena Vuckovic, and Feng Wang, "Electrical Control of Silicon Photonic Crystal Cavity by Graphene," Nano Lett., Vol. 13, 515-518, 2013;

[63] Abdul Shakoor, Roberto Lo Savio, Paolo Cardile, Simone L. Portalupi, Dario Gerace, Karl Welna, Simona Boninelli, Giorgia Franzò, Francesco Priolo, Thomas F. Krauss, Matteo Galli, and Liam O'Faolain, "Room temperature all-silicon photonic crystal nanocavity light emitting diode at sub-bandgap wavelengths," Laser & Photon. Rev., Vol. 7, No. 1, pp. 114-121, Jan. 2013;

[64] H. Kosaka, T. Kawashima, A. Tomita, M. Notomi, T. Tamamura, T. Sato, and S. Kawakami "Superprism phenomena in photonic crystals: toward microscale lightwave circuits," J. Lightwave Technol., Vol. 17, 2032-2038, 1999;

[65] H. Kosaka, T. Kawashima, A. Tomita, T. Sato, and S. Kawakami, "Photonic crystals for micro lightwave circuits using wavelength-dependent angular beam steering," Appl. Phys. Lett., Vol. 74, 1370-1372, 1999;

[66] M. Notomi, "Theory of light propagation in strongly modulated photonic crystals: Refractionlike behavior in the vicinity of the photonic band gap," Phys. Rev. B, Vol. 62, 10696-10705, 2000;

[67] Babak Momeni, Jiandong Huang, Mohammad Soltani, Murtaza Askari, Saeed Mohammadi, Mohammad Rakhshandehroo, and Ali Adibi, "Compact wavelength demultiplexing using focusing negative index photonic crystal superprisms," Opt. Exp., Vol. 14, No. 6, 2413, Mar. 2006;

[68] M. Loncar, D. Nedeljkovic, T. Doll, J. Vuckovic, A. Scherer, and T. P. Pearsall, "Waveguiding in planar photonic crystals," Appl. Phys. Lett., Vol. 77, 1937-1939, 2000;

[69] S. Y. Lin, E. Chow, S. G. Johnson, and J. D. Joannopoulos, "Demonstration of highly efficient waveguiding in a photonic crystal slab at the 1.5-mu m wavelength," Opt. Lett., Vol. 25, 1297-1299, 2000;

[70] M. Notomi, A. Shinya, K. Yamada, J. Takahashi, C. Takahashi, and I. Yokohama, "Structural tuning of guiding modes of line-defect waveguides of silicon-on-insulator photonic crystal slabs," IEEE J. Quant. Electron., Vol. 38, 736-742, 2002;

[71] W. T. Lau, and S. H. Fan, "Creating large bandwidth line defects by embedding dielectric waveguides into photonic crystal slabs," Appl. Phys. Lett., Vol. 81, 3915-3917, 2002;

[72] A. H. Atabaki, E. S. Hosseini, B. Momeni, and A. Adibi, "Enhancing the guiding bandwidth of photonic crystal waveguides on silicon-on-insulator," Opt. Lett., Vol. 33, 2608-2610, 2008;

[73] M. Soljacic, and J. D. Joannopoulos, "Enhancement of nonlinear effects using photonic crystals," Nat. Mater., Vol. 3, 211-219, 2004;

[74] T. F. Krauss, "Slow light in photonic crystal waveguides," J. of Phys. D-Appl. Phys., Vol. 40, 2666-2670, 2007;

[75] T. Baba, "Slow light in photonic crystals," Nat. Photon., Vol. 2, 465-473, 2008;

[76] Y. A. Vlasov, M. O'Boyle, H. F. Hamann, and S. J. McNab, "Active control of slow light on a chip with photonic crystal waveguides," Nat., Vol. 438, 65-69, 2005;

[77] L. L. Gu, W. Jiang, X. N. Chen, L. Wang, and R. T. Chen, "High speed silicon photonic crystal waveguide modulator for low voltage operation," Appl. Phys. Lett., Vol. 90, 071105, 2007;

[78] D. M. Beggs, T. P. White, L. O'Faolain, and T. F. Krauss, "Ultracompact and low-power optical switch based on silicon photonic crystals," Opt. Lett., Vol. 33, 147-149, 2008;

[79] Z. Yu, and S. H. Fan, "Complete optical isolation created by indirect interband photonic transitions," Nat. Photon., Vol. 3, 91-94, 2009;

[80] B. Cluzel, D. Gerard, E. Picard, T. Charvolin, V. Calvo, E. Hadji, and F. de Fornel, "Experimental demonstration of Bloch mode parity change in photonic crystal waveguide," Appl. Phys. Lett., Vol. 85, 2682-2684, 2004;

[81] E. Dulkeith, S. J. McNab, and Y. A. Vlasov, "Mapping the optical properties of slab-type two-dimensional photonic crystal waveguides," Phys. Rev. B, Vol. 72, 115102, 2005;

[82] W. Song, R. A. Integlia, and W. Jiang, "Slow light loss due to roughness in photonic crystal waveguides: An analytic approach," Phys. Rev. B, Vol. 82, 235306, 2010;

[83] With >1 μm top/bottom claddings and 6 rows of holes per side;

[84] E. Kuramochi, M. Notomi, S. Hughes, A. Shinya, T. Watanabe, and L. Ramunno, "Disorder-induced scattering loss of line-defect waveguides in photonic crystal slabs," Phys. Rev. B, Vol. 72, 161318-161314, 2005;

[85] L. O'Faolain, S. A. Schulz, D. M. Beggs, T. P. White, M. Spasenovic, L. Kuipers, F. Morichetti, A. Melloni, S. Mazoyer, J. P. Hugonin, P. Lalanne, and T. F. Krauss, "Loss engineered slow light waveguides," Opt. Exp., Vol. 18, 27627-27638, 2010;

[86] M. H. Shih, W. J. Kim, W. Kuang, J. R. Cao, H. Yukawa, S. J. Choi, J. D. O'Brien, P. D. Dapkus, and W. K. Marshall, "Two-dimensional photonic crystal Mach-Zehnder interferometers," Appl. Phys. Lett., Vol. 84, 460-462, 2004;

[87] H. H. Tao, C. Ren, Y. Z. Liu, Q. K. Wang, D. Z. Zhang, and Z. Y. Li, "Near-field observation of anomalous optical propagation in photonic crystal coupled-cavity waveguides," Opt. Exp., Vol. 18, 23994-24002, 2010;

[88] B. T. Lee, and S. Y. Shin, "Mode-order converter in a multimode waveguide," Opt. Lett., Vol. 28, 1660-1662, 2003;

[89] M. W. Pruessner, J. B. Khurgin, T. H. Stievater, W. S. Rabinovich, R. Bass, J. B. Boos, and V. J. Urick, "Demonstration of a mode-conversion cavity add-drop filter," Opt. Lett., Vol. 36, 2230-2232, 2011;

[90] J. Leuthold, P. A. Besse, E. Gamper, M. Dulk, S. Fischer, and H. Melchior, "Cascadable dual-order mode all-optical switch with integrated data- and control-signal separators," Electron. Lett., Vol. 34, 1598-1600, 1998;

[91] Y. Jiao, S. H. Fan, and D. A. B. Miller, "Demonstration of systematic photonic crystal device design and optimization by low-rank adjustments: an extremely compact mode separator," Opt. Lett., Vol. 30, 141-143, 2005;

[92] J. Y. Lee, and P. M. Fauchet, "Slow-light dispersion in periodically patterned silicon microring resonators," Opt. Lett., Vol. 37, 58-60, 2012;

[93] J. Tan, M. Lu, A. Stein, and W. Jiang, "High-purity transmission of a slow light odd mode in a photonic crystal waveguide," Opt. Lett., Vol. 37, 3189-3191, 2012;

[94] Z. Yu, and S. H. Fan, "Complete optical isolation created by indirect interband photonic transitions," Nat. Photon., Vol. 3, No. 2, 91-94, 2009;

[95] H. Lira, Z. F. Yu, S. H. Fan, and M. Lipson, "Electrically driven nonreciprocity induced by interband photonic transition on a silicon chip," Phys. Rev. Lett., Vol. 109, No. 3, 033901, 2012;

[96] Y. A. Vlasov, M. O'Boyle, H. F. Hamann, and S. J. McNab, "Active control of slow light on a chip with photonic crystal waveguides," Nat., Vol. 438, No. 7064, 65-69, 2005;

[97] L. L. Gu, W. Jiang, X. N. Chen, L. Wang, and R. T. Chen, "High speed silicon photonic crystal waveguide modulator for low voltage operation," Appl. Phys. Lett., Vol. 90, No. 7, 071105, 2007;

[98] H. C. Nguyen, Y. Sakai, M. Shinkawa, N. Ishikura, and T. Baba, "10 gb/s operation of photonic crystal silicon optical modulators," Opt. Exp., Vol. 19, No. 14, 13000-13007, 2011;

[99] B. Corcoran, M. D. Pelusi, C. Monat, J. Li, L. O'Faolain, T. F. Krauss, and B. J. Eggleton, "Ultracompact 160 gbaud all-optical demultiplexing exploiting slow light in an engineered silicon photonic crystal waveguide," Opt. Lett., Vol. 36, No. 9, 1728-1730, 2011;

[100] B. Cluzel, D. Gerard, E. Picard, T. Charvolin, V. Calvo, E. Hadji, and F. de Fornel, "Experimental demonstration of bloch mode parity change in photonic crystal waveguide," Appl. Phys. Lett., Vol. 85, No. 14, 2682-2684, 2004;

[101] J. Tan, M. Lu, A. Stein, and W. Jiang, "High-purity transmission of a slow light odd mode in a photonic crystal waveguide," Opt. Lett., Vol. 37, No. 15, 3189-3191, 2012;

[102] W. Song, R. A. Integlia, and W. Jiang, "Slow light loss due to roughness in photonic crystal waveguides: An analytic approach," Phys. Rev. B, Vol. 82, No. 23, 235306, 2010;

[103] R. A. Integlia, W. Song, J. Tan, and W. Jiang, "Longitudinal and angular dispersions in photonic crystals: A synergistic perspective on slow light and superprism effects," J Nanosci. and Nanotech., Vol. 10, No. 3, 1596-1605, 2010;

[104] A. H. Atabaki, E. S. Hosseini, B. Momeni, and A. Adibi, "Enhancing the guiding bandwidth of photonic crystal waveguides on silicon-on-insulator," Opt. Lett., Vol. 33, No. 22, 2608-2610, 2008;

[105] R. A. Soref, and B. R. Bennett, "Electrooptical effects in silicon," IEEE J. Quantum Electron., Vol. 23, No. 1, 123-129, 1987;

[106] M. Soljacic, and J. D. Joannopoulos, "Enhancement of nonlinear effects using photonic crystals," Nat. Mater., Vol. 3, No. 4, 211-219, 2004;

[107] Y. Q. Jiang, W. Jiang, L. L. Gu, X. N. Chen, and R. T. Chen, "80-micron interaction length silicon photonic crystal waveguide modulator," Appl. Phys. Lett., Vol. 87, No. 22, 221105, 2005;

[108] W. Jiang, L. Gu, X. Chen, and R. T. Chen, "Photonic crystal waveguide modulators for silicon photonics: Device physics and some recent progress," Solid-State Electron., Vol. 51, 1278-1286, 2007;

[109] M. Chahal, G. K. Celler, Y. Jaluria, and W. Jiang, "Thermo-optic characteristics and switching power limit of slow-light photonic crystal structures on a silicon-on-insulator platform," Opt. Exp., Vol. 20, No. 4, 4225-4231, 2012;

[110] E. Kuramochi, M. Notomi, S. Hughes, A. Shinya, T. Watanabe, and L. Ramunno, "Disorder-induced scattering loss of line-defect waveguides in photonic crystal slabs," Phys. Rev. B, Vol. 72, No. 16, 161318, 2005;

[111] S. Combrie, N. V. Q. Tran, E. Weidner, A. De Rossi, S. Cassette, P. Hamel, Y. Jaouen, R. Gabet, and A. Talneau, "Investigation of group delay, loss, and disorder in a photonic crystal waveguide by low-coherence reflectometry," Appl. Phys. Lett., Vol. 90, No. 23, 231104, 2007;

[112] M. S. Kang, A. Butsch, and P. S. J. Russell, "Reconfigurable light-driven opto-coustic isolators in photonic crystal fibre," Nat. Photon., Vol. 5, No. 9, 549-553, 2011;

[113] A. Hosseini, X. C. Xu, H. Subbaraman, C. Y. Lin, S. Rahimi, and R. T. Chen, "Large optical spectral range dispersion engineered silicon-based photonic crystal waveguide modulator," Opt. Exp., Vol. 20, No. 11, 12318-12325, 2012;

[114] R. Soref, "Mid-infrared photonics in silicon and germanium," Nat. Photon., Vol. 4, No. 8, 495-497, 2010;

[115] Jun Tan, Richard A. Soref, and Wei Jiang, Interband scattering in a slow light photonic crystal waveguide under electro-optic tuning, Opt. Exp., Vol. 21, No. 6, Mar. 2013;

[116] J. B. Pendry, "Negative Refraction Makes a Perfect Lens," Phys. Rev. Lett., Vol. 85, No. 18, pp. 3966, Oct. 2000;

[117] Nicholas Fang, Hyesog Lee, Cheng Sun, Xiang Zhang, "Sub–Diffraction-Limited Optical Imaging with a Silver Superlens," Science, Vol. 308, pp. 534, Apr. 2005;

[118] Pratik Chaturvedi, Wei Wu, V.J. Logeeswaran, Zhaoning Yu, M. Saif Islam, S. Y. Wang, R. Stanley Williams, and Nicholas X. Fang, "A smooth optical superlens," Appl. Phys. Lett., Vol. 96, 043102, 2010;

[119] Hong Liu, Bing Wang, Lin Ke, Jie Deng, Chan Choy Chum, Siew Lang Teo, Lu Shen, Stefan A. Maier, and Jinghua Teng, "High Aspect Subdiffraction-Limit Photolithography via a Silver Superlens," Nano Lett., Vol. 12, pp. 1549-1554, 2012;

[120] Alina Schilling, Joerg Schilling, Carsten Reinhardt, and Boris Chichkov, "A superlens for the deep ultraviolet," Appl. Phys. Lett., Vol. 95, 121909, 2009;

[121] Zhong Shi, Vladimir Kochergin, and Fei Wang, "193nm Superlens Imaging Structure for 20nm Lithography Node," Opt. Exp., Vol. 17, No. 14, pp. 11309, 2009;

[122] Zhong Shi, Vladimir Kochergin, and Fei Wang, "Depth-of-focus (DoF) analysis of a 193nm superlens imaging structure," Opt. Exp., Vol. 17, No. 22, pp. 20538, 2009;

[123] E. D. Palik, "Handbook of Optical Constants of Solids," Academic Press, 1998;

[124] Jun Tan, and Wei Jiang, "Monthly report of the superlens project to Luna Innovations, Inc." 2011~2012;

[125] http://docs.lumerical.com/en/mode/user_guide_understanding_poynting_vector.html

[126] Nicholas Fang, Zhaowei Liu, Ta-Jen Yen, and Xiang Zhang, "Regenerating evanescent waves from a silver superlens," Opt. Exp., Vol. 11, No. 7, Apr. 2003;

[127] J. Tan, B. Dickerson, B. Chang, Z. Wang, Q. Zou, and W. Jiang, "193nm photolithography with plasmonic superlens," manuscript in preparation.

CURRICULUM VITAE
OF
JUN TAN

EDUCATION

October 2013   **Doctor of Philosophy**
                    Rutgers University, New Brunswick, NJ, USA

June 2008   **Master of Science**
                    Shanghai Institute of Technical Physics, CAS, Shanghai, China

June 2005   **Bachelor of Science**
                    Nanjing University, Nanjing, China

EXPERIENCE

Research Assistant   2008-2013
    Photonics Lab, Rutgers University

Teaching Assistant   2010-2012
    Department of Electrical and Computer Engineering, Rutgers University

JOURNAL PUBLICATIONS

[1] **Jun Tan**, Richard A. Soref, and Wei Jiang, *Interband scattering in a slow light photonic crystal waveguide under electro-optic tuning*, **Optics Express**, Vol. 21, No. 6, 6756~6763, Mar. 2013.

[2] **Jun Tan**, Ming Lu, Aaron Stein, and Wei Jiang, *High-purity transmission of a slow light odd mode in a photonic crystal waveguide*, **Optics Letters**, Vol. 37, No. 15, 3189~3191, Aug. 2012.

[3] **Jun Tan**, Weiwei Song, and Wei Jiang, *Anomalous Propagation in Low Index Contrast Metamaterials: Assessment of the Beam Collimation Condition*, **International Journal of Optics**, Vol. 2012, Article ID 120731.

[4] **Jun Tan**, Yonggang Yuan, Xiangyang Li, *Small pixel area design of GaN UV FPA ROIC with CTIA structure and simulation*, **Laser & Infrared**, Vol. 38, No. 6, Jun. 2008.

[5] Lianghong Yin, Ming Lu, Leszek Wielunski, Weiwei Song, **Jun Tan**, Yicheng Lu, and Wei Jiang, *Fabrication and characterization of compact silicon oxynitride waveguides on silicon chips*, **Journal of Optics**, Vol. 14, 085501, 2012.

[6] Ryan A. Integlia, Weiwei Song, Jun Tan, and Wei Jiang, *Longitudinal and Angular Dispersions in Photonic Crystals: A Synergistic Perspective on Slow Light and Superprism Effects*, **Journal of Nanoscience and Nanotechnology**, Vol. 10, Issue 3, 2010.